República Federativa do Brasil
Ministério do Desenvolvimento, Indústria e do Comércio Exterior
Instituto Nacional da Propriedade Industrial

(11) (21) **PI 0406270-1 A**

(22) Data de Depósito: 30/12/2004
(43) Data de Publicação: **22/08/2006**
(RPI 1859)

(51) Int. Cl^7.:
C01G 49/08

(54) Título: **PROCESSO PARA ESTABILIZAÇÃO DA MAGNETITA OBTIDA ATRAVÉS DA REDUÇÃO QUÍMICA DA HEMATITA**

(71) Depositante(s): Universidade Federal de Minas Gerais (BR/MG)

(72) Inventor(es): José Domingos Fabris, João Hebert Moreira Viana, Márcio César Pereira, Claudia Martins Tavares

(57) Resumo: "PROCESSO PARA ESTABILIZAÇÃO DA MAGNETITA OBTIDA ATRAVÉS DA REDUÇÃO QUÍMICA DE HEMATITA". A presente invenção trata de um processo para estabilização de magnetita (fórmula química ideal, Fe_3O_4) finamente dividida, obtida a partir da redução química de Fe^{3+} de hematita (fórmula química ideal, α-Fe_2O_3), usando-se, como fonte redutora, o carvão, de qualquer origem, sob aquecimento a uma temperatura entre 300°C e 800°C. O processo de estabilização da magnetita formada consiste na imersão do material, imediatamente após o tratamento térmico, em glicerina ($CH_2OHCHOHCH_2OH$, propano-1,2,3-triol), que previne o contato com o ar e a oxidação da magnetita formada, permitindo sua utilização em processos catalíticos ou outras aplicações que exijam pequeno tamanho de partícula, alta reatividade e exposição da superfície ativa e não oxidada da magnetita. O processo leva à formação de uma camada protetora por ação da glicerina, que pode ser eventualmente removida, se conveniente, para uso em processos catalíticos heterogêneos.

 PI0406270

PROCESSO PARA ESTABILIZAÇÃO DA MAGNETITA OBTIDA ATRAVÉS DA REDUÇÃO QUÍMICA DE HEMATITA

Refere-se o presente pedido de patente a um processo para estabilização da magnetita (fórmula química ideal, Fe_3O_4), a partir da redução química da hematita (fórmula química ideal, α-Fe_2O_3), proveniente de fontes sintéticas ou naturais, como minério de ferro, cangas, rejeitos industriais ou solo, usando-se como agente redutor o carvão de qualquer origem (mineral, vegetal ou animal), mantidos em contato sob temperaturas entre 300°C e 800°C. Com o processo, obtém-se magnetita de alta reatividade, adequada à utilização em reações catalíticas ou em outras aplicações, que exigem pequeno tamanho de partícula e exposição da superfície ativa da magnetita, sem formação de produtos de oxidação, particularmente com reformação de hematita, por contato com o ar. O processo de estabilização garante a manutenção da reatividade, por prevenir a formação dessa camada oxidada na superfície do material, como costuma ocorrer nas condições tradicionais da síntese, até o uso final.

A redução da hematita por aquecimento em meio com um agente redutor, como os gases provenientes da combustão do carvão em atmosfera de ar, é uma reação relativamente bem conhecida, partindo dos processos de redução do ferro para fins metalúrgicos. Existem várias patentes relativas ao uso ou otimização de processos correlatos, como a patente intitulada "*Process for reducing the ferric oxides content of ferruginous ore materials*" N. 26047/1948, ou a patente "*Process for the preliminary treatment of iron ore*" N. 15301/1961. Entretanto, a magnetita com pequeno tamanho de partícula (<1 micrômetro), obtida por processos convencionais, sofre oxidação durante o resfriamento e exposição ao ar, transformando-se parcialmente em hematita, que capeia as partículas formadas, inviabilizando, assim, a utilização desse material em processos que exigem a exposição da superfície ativa da magnetita, como nas reações de catálise heterogênea. A estabilização da magnetita tem sido objeto de patentes para outros fins, como produção de pigmentos para tintas e de mídia magnética. A patente "*Estabilization of magnetite pigments with heterocyclic nitrogen compounds*" N. 944501/1978

propõe um processo para estabilização de pigmentos de magnetita finamente divididos contra a oxidação utilizando compostos nitrogenados heterocíclicos, como morfolina, piperazina, piperidina ou seus derivados. Nesses casos, os centros reativos da superfície ativa (Fe^{3+}/Fe^{2+}), que são responsáveis pela ação catalítica e também pela instabilidade oxidativa ao ar, são desativados, pela adsorção daqueles compostos nitrogenados heterocíclicos, inviabilizando sua utilização em processos catalíticos. Em outro caso, a patente *"Magnetite coating composition"* N. 54752/1973, relativa à produção de pigmentos para tinta de impressão à base de magnetita, usa óleos secativos, como o de linhaça, para a cobertura das partículas coloidais formadas por reação em meio aquoso, promovendo seu isolamento, após reação com amônia. Nesse caso também, ocorre o isolamento dos sítios ativos em reações catalíticas, da superfície dos grãos. De acordo com os autores do artigo publicado no *Journal of Materials Chemistry* 13 (8): 1983-1987, 2003, é possível sintetizar nanopartículas de magnetita através da redução de $Fe(acac)_3$ (acac = acetilacetonato), na presença de etilenoglicol, ácido oléico e óxido de trioctilfosfina ou hexadecilamina como estabilizantes.

A oxidação da magnetita ao ar é um processo rápido e espontâneo, especialmente em se tratando de materiais de grande superfície específica e de alta reatividade, como aqueles utilizados para catálise. Isto torna o processo dependente da exclusão do contato com o oxigênio do ar, que deve ser efetuado concomitantemente com a síntese ou imediatamente após. Com o intuito de proteger quimicamente a magnetita contra oxidação, desenvolveu-se o processo de isolamento contra a ação do oxigênio, que é o principal agente oxidante, durante o resfriamento da amostra ao ar. O processo consiste na imediata imersão da magnetita, ainda quente, após o tratamento redutivo da hematita a temperaturas entre 300 °C e 800 °C, em glicerina ($CH_2OHCHOHCH_2OH$, propano-1, 2, 3- triol). A camada de glicerina cria uma película de proteção e previne o contato direto do material obtido com o ar, preservando assim o Fe^{2+} na estrutura da magnetita. Essa camada pode ser removida posteriormente de forma simples, na preparação do material para uso

em processos de catálise, permitindo a exposição dos centros reativos da superfície ativa da magnetita.

A preservação do Fe^{2+} na estrutura da magnetita poderá ser melhor compreendido através da seguinte descrição detalhada, em consonância com os espectros Mössbauer representados na Figura 1 em anexo.

Figura a): espectro experimental Mössbauer de uma amostra de hematita ***(Hm)***, que é um óxido de ferro com apenas ferro no estado de oxidação 3+, na estrutura cristalina. Nenhuma linha de ressonância de Fe^{2+} é observada no espectro.

Figura b): espectro experimental Mössbauer da mesma amostra de hematita desta vez reduzida com carvão, sem a camada de glicerina para a proteção da superfície ativa da magnetita formada, contra oxidação e reformação de hematita. A magnetita é um óxido de ferro com estrutura de espinélio invertido, com um sítio de coordenação ferro-oxigênio, de simetria tetraédrica, simbolicamente representado por ***T***, e outro de coordenação octaédrica, representado por ***M***. No sítio tetraédrico, a magnetita tem apenas ferro no estado de oxidação 3+, enquanto que no sítio octaédrico ocorre ferro nos estados de oxidação 2+ e 3+. Analisando o espectro obtido, podemos observar a presença dos sítios tetraédrico ***(T)*** e octaédrico ***(M)*** da magnetita, com linhas relativamente incipientes. A intensidade da linha de ressonância correspondente ao sítio octaédrico é representada pela seta entre as linhas pontilhadas. Assim, conclui-se que parte significativa do Fe^{2+} gerado pela redução com carvão foi oxidado, como fica evidenciado pelas linhas de ressonância pouco intensas, relativas ao sítio ***M***.

Figura c): espectro experimental Mössbauer da mesma amostra de hematita, desta vez, reduzida com carvão e protegida contra a oxidação do Fe^{2+}, pela camada de glicerina. Pode-se observar que as linhas de ressonância do sítio ***(M)*** são agora muito mais intensas do que as do espectro anterior, o que indica que a preservação do Fe^{2+} com glicerina é realmente eficiente.

O processo para obtenção da magnetita estabilizada divide-se em duas etapas. A primeira etapa consiste na redução da hematita, de qualquer origem, sintética ou natural. A segunda etapa consiste na estabilização da

PI0406270

magnetita obtida, por imersão imediata da mistura ainda quente, como resultado do tratamento térmico, de magnetita e carvão residual da reação de redução, diretamente em glicerina.

ETAPA 1: OBTENÇÃO DA MAGNETITA A PARTIR DA HEMATITA

Amostras sintéticas ou naturais de hematita são misturadas com carvão, de qualquer origem (vegetal, animal ou mineral), na proporção em massa de 1:5 amostra:carvão e colocadas em mufla, por um período entre uma e duas horas, a uma temperatura fixada, no intervalo entre 300 °C e 800 °C. Quando aquecidas, as partículas do carvão sofrem volatilização, produzindo coque sólido, alcatrão e gases leves, como ilustrado pela reação (*Thermochimica Acta 410 (2004) 133-140*):

$$\text{Carvão} \xrightarrow{\Delta} \text{coque} + \text{alcatrão} + \text{gases}$$ (e.g. H_2, CO)

Desse modo, esses gases produzidos durante a volatilização do carvão são capazes de reduzir hematita sintética ou natural, de acordo com as equações abaixo:

$$3Fe_2O_3 + CO \rightarrow 2Fe_3O_4 + CO_2$$

$$3Fe_2O_3 + H_2 \rightarrow 2Fe_3O_4 + H_2O$$

ETAPA 2: ESTABILIZAÇÃO DA MAGNETITA FORMADA

Após o término da redução da hematita a magnetita, retira-se o material obtido, da mufla. Durante o resfriamento, se o material obtido é constituído por partículas finamente divididas e não está protegido contra o oxigênio do ar, ocorre a oxidação do ferro, na superfície da magnetita, re-formando uma camada de hematita, que passa a capear os grãos de magnetita. A oxidação da magnetita é representada pela equação:

$$2Fe_3O_4 + \frac{1}{2}O_2 \rightarrow 3Fe_2O_3$$

Para evitar essa reação, foi proposta a imersão imediata da magnetita, ainda quente, em glicerina, até que o equilíbrio térmico seja atingido. A glicerina forma uma película protetora sobre a superfície da magnetita, impedindo o contato desta com o ar e, conseqüentemente prevenindo a oxidação a hematita.

PI0406270

REIVINDICAÇÕES

PROCESSO PARA ESTABILIZAÇÃO DA MAGNETITA OBTIDA ATRAVÉS DA REDUÇÃO QUÍMICA DE HEMATITA

1. PROCESSO PARA ESTABILIZAÇÃO DA MAGNETITA OBTIDA ATRAVÉS DA REDUÇÃO QUÍMICA DE HEMATITA, proveniente de fontes sintéticas ou naturais, como minério de ferro, cangas, rejeitos industriais ou solo, caracterizado pela utilização de glicerina como meio de resfriamento do material termicamente tratado, a fim de proteger e prevenir a re-oxidação do Fe^{2+} da magnetita, de partículas finamente divididas, por contato de todo o conjunto com qualquer atmosfera oxidante, como o ar.

P1040270

Figura

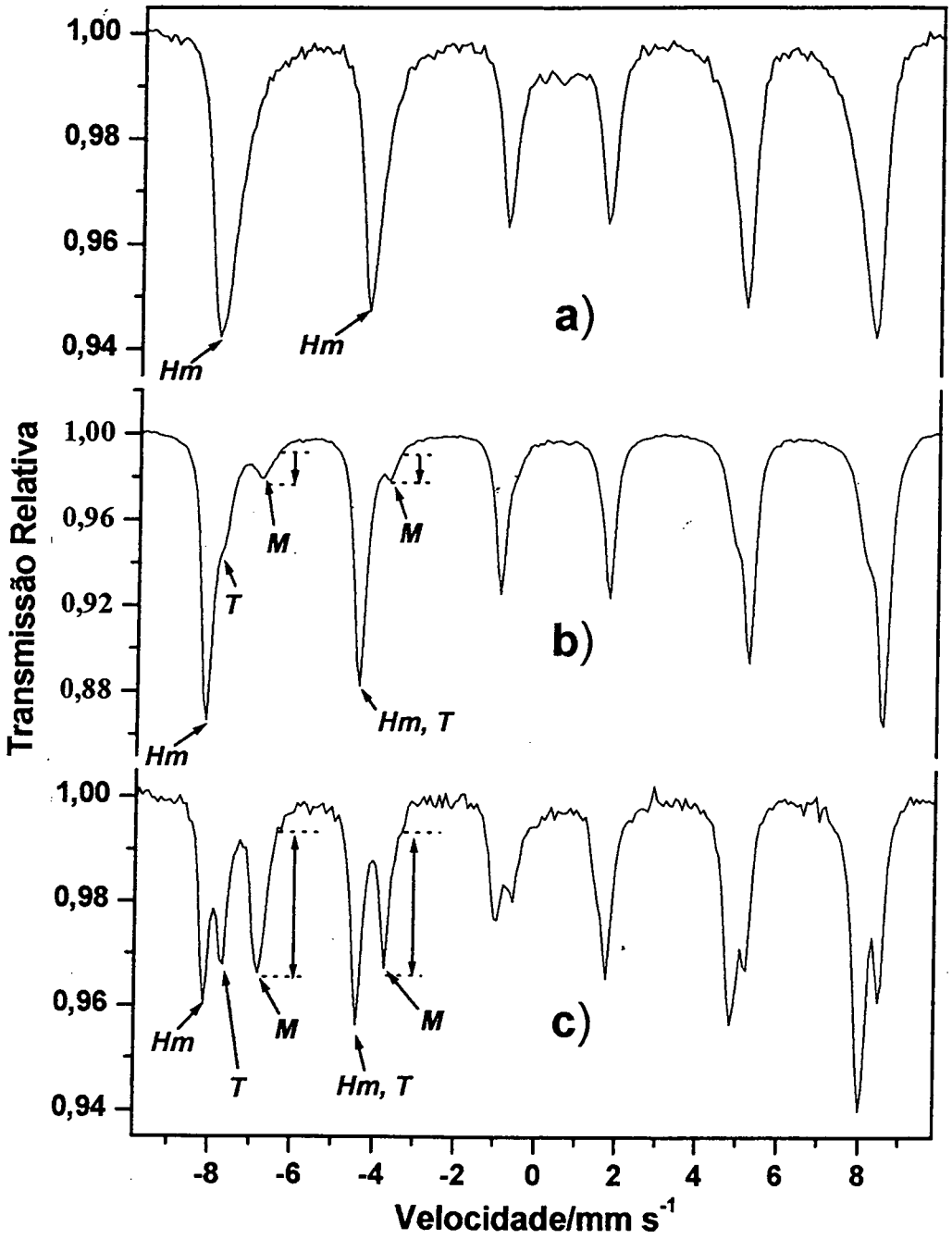

PI0406270

RESUMO

PROCESSO PARA ESTABILIZAÇÃO DA MAGNETITA OBTIDA ATRAVÉS DA REDUÇÃO QUÍMICA DE HEMATITA

A presente invenção trata de um processo para estabilização de magnetita (fórmula química ideal, Fe_3O_4) finamente dividida, obtida a partir da redução química de Fe^{3+} de hematita (fórmula química ideal, α-Fe_2O_3), usando-se, como fonte redutora, o carvão, de qualquer origem, sob aquecimento a uma temperatura entre 300 °C e 800 °C. O processo de estabilização da magnetita formada consiste na imersão do material, imediatamente após o tratamento térmico, em glicerina ($CH_2OHCHOHCH_2OH$, propano-1, 2, 3- triol), que previne o contato com o ar e a oxidação da magnetita formada, permitindo sua utilização em processos catalíticos ou outras aplicações que exijam pequeno tamanho de partícula, alta reatividade e exposição da superfície ativa e não oxidada da magnetita. O processo leva à formação de uma camada protetora por ação da glicerina, que pode ser eventualmente removida, se conveniente, para uso em processos catalíticos heterogêneos.

República Federativa do Brasil
Ministério do Desenvolvimento, Indústria e do Comércio Exterior
Instituto Nacional da Propriedade Industrial.

(21) **PI0904098-6 A2**

(22) Data de Depósito: 02/10/2009
(43) Data da Publicação: 14/06/2011
(RPI 2110)

(51) Int.Cl.:
B22F 1/02 2006.01
B22F 9/20 2006.01

(54) Título: **PROCESSO DE OBTENÇÃO DE PARTÍCULAS MAGNÉTICAS RECOBERTAS POR CARBONO**

(73) Titular(es): Universidade Federal de Minas Gerais

(72) Inventor(es): Aline Almeida da Silva Oliveira, José Domingos Ardisson, Juliana Cristina Tristão, Marcelo Gonçalves Rosmaninho, Rochel Montero Lago

(57) Resumo: Processo de Obtenção de Partículas Magnéticas Recobertas por Carbono. A presente invenção descreve um processo para a produção de particulas magnéticas recobertas por carbono para serem utilizadas em aplicações tecnológicas. O caráter inovador desta invenção está na simplicidade e no baixo custo do processo que permite utilizar diversas fontes de ferro, tais como de origem sintética (α-Fe_2O_3, Fe_3O_4 e FeOOH), natural (minérios) ou rejeitos industriais (lama vermelha, rejeito de aciaria, rejeitos siderúrgicos). O recobrimento de carbono é realizado através de um processo de etapa única que envolve a redução dos áxidos de ferro para formar o núcleo magnético e deposição de carbono a partir de diferentes tipos de compostos orgânicos que também são insumos disponíveis e de baixo custo tais como metano e etanol.

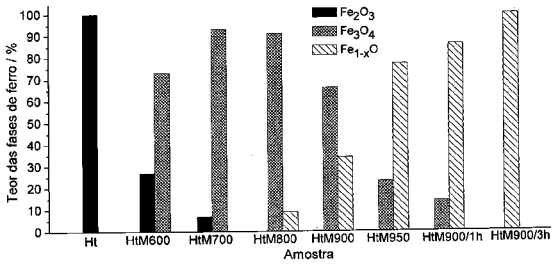

PI0904098-6

Processo de Obtenção de Partículas Magnéticas Recobertas por Carbono

Campo da invenção

A presente invenção descreve um processo simples e de baixo custo para obtenção de partículas magnéticas recobertas por carbono para serem utilizadas como materiais magnéticos em aplicações industriais como adsorventes e suportes de catalisadores. Pela presente tecnologia aqui descrita, é possível se utilizar diversas fontes de ferro, como principal constituinte dos núcleos magnéticos, tais como de origem sintética (α-Fe_2O_3, Fe_3O_4 e FeOOH), natural (minérios) ou mesmo rejeitos industriais (lama vermelha, rejeito de aciaria, rejeitos siderúrgicos). Na presente invenção a fonte de ferro é reduzida para formar a fase magnética e recoberta por carbono em apenas uma etapa, utilizando para isso diferentes tipos de compostos orgânicos tais como metano e etanol.

Estado da técnica

Partículas magnéticas, especialmente nanopartículas, mostram um enorme potencial para diversas aplicações. Os principais setores de mercado identificados para as partículas magnéticas são: indústrias de química fina, petroquímicas, indústria de defensivos agrícolas, indústria de essências e aromas, indústria farmacêutica e empresas ambientais. Algumas destas aplicações incluem processos de descontaminação ambiental, ex. uso de nanopartículas de Fe_3O_4/SiO_2 modificada por surfactantes para remoção de compostos fenólicos da água, nanocompósitos de ferro/óxido de ferro usados para remediação de contaminação ambiental e o uso de nanopartículas de Fe^0 e Fe/Pd para degradação de compostos organoclorados e na remoção de metais pesados como As^{3+}, As^{5+}, Cr^{6+} e Pb^{2+}. Outras aplicações se encontram na área de catálise. Estima-se que o mercado brasileiro de catalisadores, em geral, gire em torno de 40 mil toneladas de catalisadores por ano. Dentro do mercado de catalisadores pode-se dividi-lo em quatro grandes tipos: catalisadores para refino de petróleo (97% do mercado), para química fina, para produção de polímeros e outras aplicações diversas.

Segundo a Fábrica Carioca de Catalisadores (FCC), empresa composta por uma sociedade entre a Petrobrás e a Albemarle Corporation, o mercado latino-americano de catalisadores para refino de petróleo representa um volume de vendas de 33 mil toneladas por ano e faturamento de US$ 70 milhões. Só as refinarias brasileiras consomem 28 mil toneladas de catalisadores por ano. As 5 mil toneladas restantes são vendidas nos mercados argentino, uruguaio, colombiano, peruano e cubano. Segundo a FCC e a BCC Research, o mercado mundial desse tipo de catalisador gera uma receita anual superior a US$ 2,7 bilhões, ou seja, o mercado brasileiro representa menos de 4% do mercado mundial. De acordo com a BCC Research, desde 2005 o mercado mundial de catalisadores tem crescido a uma taxa de 5,8% ao ano. A expectativa é que até o ano de 2010 esse mercado chegue a US$ 3,5 bilhões. É possível observar também recentes e novos investimentos no mercado de catálise. Em 2005 a FCC investiu cerca de US$ 40 milhões com objetivo de aumentar a produção para 45 mil toneladas de catalisadores de refino por ano.

Algumas aplicações encontradas na área de catálise no estado da arte são a recuperação de catalisadores de Rh(0) suportados em Fe_3O_4/SiO_2 em reações de hidrogenação, estudo da atividade catalítica de Pd suportado em nanopartículas magnéticas recobertas por carbono em reações Heck e o preparo de catalisadores ácidos sulfônicos suportados em nanopartículas magnéticas recobertas por sílica (Jacinto, M.J.; Kiyohara, P.K.; Masunaga, S.H.; Jardim, R.F.;Rossi, L.M. *Applied Catalysis a-General.* 338, 52-57, 2008, Shen, B.; Li, Y.; Wang, Z.F.;He, N.Y. *Chinese Journal of Catalysis.* 28, 509-513, 2007 e Gill, C.S.; Price, B.A.; Jones, C.W. *Journal of Catalysis.* 251, 145-152, 2007).

Grande parte das aplicações descritas na literatura, especialmente para as nanopartículas, destina-se a usos na biomedicina. Alguns exemplos são: no estudo da biocompatibilidade de nanopartículas de óxidos de ferro recobertas com dextrina, nanopartículas de Fe^0 recobertas com Fe_xO_y, FePt ou Pt para estudos biomédicos, uso de óxidos de ferro recobertos pelo biopolímero quitosana em aplicações terapêuticas como hipertermia e liberação de drogas, nanopartículas de Fe^0 encapsuladas por carbono para liberação de drogas, uso

como agente de contraste em imagens de ressonância magnética por nanopartículas superparamagnéticas baseadas em ferro recobertas com galactose, recobertas por carbono e carbono/sílica e recobertas por Au/SiO_2, entre outros.

No estado da técnica foram encontrados métodos de produção de partículas magnéticas recobertas com diversos materiais, tais como polímeros sintéticos, polissacarídeos ou poliaminoácidos (EP2000484 (A1), KR20080084102 (A), WO2007095871 (A2)) e compostos orgânicos do tipo uréia, tiuréia, isocianato ou isotiocianato e sais de ácidos graxos como estearato de sódio, oleato, linoleato, linolenato e ricisoleato (GB1532970 (A), GB1450241 (A)). Nesta busca, foram encontradas aplicações biomédicas como agente de contraste, material para transporte de drogas, termoterapia, diagnóstico e tratamento do câncer (EP1842554 (A1), EP1810688 (A1), WO2007095871 (A2)) e em muitos casos como meio de gravação magnética de mídia (GB1532970 (A), GB1450241 (A), EP1800774 (A2), JP4246475 (A)).

Os pedidos de patentes supracitados são enumeradas a seguir:

- Metal particles coated with organic compounds – 1978 – GB1532970 (A)
- Methods of making magnetic metal particles coated with a protective layer – 1976 – GB1450241 (A)
- Fine composite metal particles and magnetic beads – 2007 – EP1800774 (A2)
- Synthesis method of metallic oxide coated dissimilar metal TM core/shell nano-particles – 2009 – CN101362200 (A)
- Process for producing polymer-coated ferromagnetic particle, and polymer-coated ferromagnetic particle – 2008 – EP2000484 (A1)
- Magnetic nano-particles coated polymer and preparation method of the same – 2008 – KR20080084102 (A)
- Coated magnetic particle containing preparation, process for producing the same and diagnostic therapeutic system – 2007 – EP1842554 (A1)
- Pharmaceutical preparation containing coated magnetic particles and method for production thereof, and diagnosis therapy system – 2007 – EP1810688 (A1)

- Superparamagnetic nanoparticles based on iron oxides with modified surface, method of their preparation and application – 2007 – WO2007095871 (A2)
- Production of magnetic coating material – 1997 – JP9180157 (A)
- Production of magnetic coating material – 1992 – JP4246475 (A)

Materiais magnéticos recobertos por carbono têm sido bastante investigados, devido à estabilidade química e térmica de estruturas de carbono e à possibilidade de produzir materiais com elevada área superficial. Diferentes tipos de carbono podem ser produzidos, tais como carbono amorfo, grafite ou mesmo nanotubos. Alguns pedidos de patentes que descrevem materiais magnéticos à base de carbono são: preparo de partículas de Co depositadas em um substrato de Si recobertas por carbono no topo de NTC (nanotubos de carbono) alinhados perpendicularmente ao substrato (CN101348936 (A)), partículas a base de metais do tipo Fe, Co ou Ni misturados com materiais a base de carbono e aquecidos em condições drásticas entre 1600 e 2800°C sob atmosfera inerte (JP9143502 (A)), nanopartículas de Fe encapsuladas com NTC pelo método da irradiação por microondas usando ferroceno (MXNL06000010 (A)), material formado por partículas contendo uma liga magnética mais carbon black (JP9180157 (A)) e compósitos formados por núcleos a base de ferro, níquel, cobalto recobertos por uma camada composta principalmente por carbono e nitreto de boro (EP1800774 (A2)).

Os seguintes depósitos de patentes descritos acima são enumerados a seguir:

- Orientational alignment carbon nano-tube and carbon coating cobalt nano-particle complex and preparation thereof – 2009 – CN101348936 (A)
- Graphite coated metallic particle and its production – 1997 – JP9143502 (A)
- Method for obtaining multilayer carbon nanotubes by microwave irradiation, which are aligned with encapsulated iron particles – 2007 MX2006NL00010–(A)
- Production of magnetic coating material – 1997 – JP9180157 (A)

- Fine composite metal particles and magnetic beads – 2007 – EP1800774 (A2)

Atualmente, vários métodos de produção e encapsulamento de partículas magnéticas com carbono são apresentados no estado da arte e da técnica. Em geral, estes processos são voltados para a produção de nanopartículas sendo processos complexos e de alto custo. Alguns exemplos são:

- descarga de arco convencional e modificado, (Dong, X.L.; Zhang, Z.D.; Jin, S.R.;Kim, B.K. *Journal of Applied Physics.* 86, 6701-6706, 1999 e Ling, J.; Liu, Y.; Hao, G.M.;Zhang, X.G. *Materials Science and Engineering B-Solid State Materials for Advanced Technology.* 100, 186-190, 2003)
- condensação química a vapor, (Enz, T.; Winterer, M.; Stahl, B.; Bhattacharya, S.; Miehe, G.; Foster, K.; Fasel, C.;Hahn, H. *Journal of Applied Physics.* 99, 4, 2006).
- deposição química a vapor (CN101348936 (A), JP9143502 (A)),
- pirólise/termólise de complexos metálicos, (Panchakarla, L.S.;Govindaraj, A. *Bulletin of Materials Science.* 30, 23-29, 2007.)
- redução química de cátions metálicos, (Jeyadevan, B.; Suzuki, Y.; Tohji, K.;Matsuoka, I. *Materials Science and Engineering a-Structural Materials Properties Microstructure and Processing.* 217, 54-57, 1996).
- reações explosivas, síntese por carbonização, (Wu, W.Z.; Zhu, Z.P.; Liu, Z.Y.; Xie, Y.I.; Zhang, J.;Hu, T.D. *Carbon.* 41, 317-321, 2003.)
- descarga de plasma (CN101362200 (A)),
- reação hidrotérmica, (Wang, Z.F.; Mao, P.F.;He, N.Y. *Carbon.* 44, 3277-3284, 2006).
- pirólise a laser (Veintemillas-Verdaguer, S.; Leconte, Y.; Costo, R.; Bomati-Miguel, O.; Bouchet-Fabre, B.; Morales, M.P.; Bonville, P.; Perez-Rial, S.; Rodriguez, I.;Herlin-Boime, N. *Journal of Magnetism and Magnetic Materials.* 311, 120-124, 2007) e
- irradiação por microondas (MXNL06000010 (A)).

Problemas do estado da técnica:

Atualmente, vários métodos de produção e encapsulamento de partículas magnéticas com carbono são apresentados no estado da arte e da técnica. Em geral, estes processos são voltados para a produção de nanopartículas, mas ainda apresentam pontos deficientes. São processos complexos tecnicamente que utilizam substâncias e precursores especiais que tornam o processo industrial complexo tecnicamente e de alto custo.

Vantagens da tecnologia

A presente invenção descreve um processo para a produção de partículas magnéticas à base de ferro/óxidos de ferro recobertas com carbono em diferentes faixas de tamanho, ex. micro e nanométrico. Os aspectos inovadores da presente invenção são:

(i) não necessita qualquer preparo especial de um precursor magnético, permitindo em princípio a utilização de qualquer tipo de óxido de ferro (magnético ou não), tais como óxidos de origem sintética (α-Fe_2O_3, Fe_3O_4 e FeOOH), óxidos naturais (minérios como hematita, magnetita e itabirito) ou rejeitos industriais (ex. lama vermelha e rejeito de aciaria);

(ii) pode utilizar uma enorme variedade de fontes de carbono como metano, etanol, tolueno ou qualquer outro composto orgânico.

(iii) permite separar as partículas magnéticas em faixas de tamanho através de um processo de decantação controlada em fluídos.

Descrição detalhada das figuras

Figura 1 - Teores das fases de ferro em diferentes temperaturas de reação da hematita com metano. Ht = hematita antes da reação; HtM = hematita após a reação com metano.

Figura 2 - Histograma da distribuição de tamanho de partícula para as partículas em suspensão obtidas para as amostras da reação da hematita com metano a 700°C (HtM700) e 950°C (HtM950). Aumento de 20000 x.

Figura 3 - Teores das fases de ferro em diferentes temperaturas de reação da hematita com etanol. Ht = hematita antes da reação; HtEt = hematita após a reação com etanol.

Figura 4 - Imagens obtidas por microscopia eletrônica de varredura (a) e de transmissão (b) para os materiais produzidos após reação entre hematita e etanol.

Figura 5 - Teores das fases de ferro obtidos após reação entre goetita, maghemita ou magnetita e etanol a 900°C (obtidos por espectroscopia Mossbauer).

Figura 6 - Teores das fases de ferro obtidos após reação entre lama vermelha e etanol em diferentes temperaturas (obtidos por espectroscopia Mossbauer). Lv = lama vermelha pura; LvEt = lama vermelha após reação com etanol.

Descrição detalhada da invenção

O processo de preparo das partículas magnéticas recobertas por carbono pode ser descrito como: (i) aquecimento dos materiais à base de óxidos de ferro em um forno a temperaturas entre 350-900°C, (ii) introdução de quantidades controladas de uma fonte de carbono que entrará em contato com todo o material à base de óxido de ferro, (iii) redução dos óxidos de ferro pela fonte de carbono para formar as fases magnéticas (que podem ser Fe metálico ou magnetita) e (iv) recobrimento das partículas magnéticas por deposição de carbono.

Os materiais descritos na invenção ora proposta podem ser utilizados como adsorventes magnéticos de contaminantes orgânicos como compostos oleosos, organoclorados e corantes (azul de metileno, vermelho drimarem,

índigo carmim) e como suporte de catalisadores metálicos como ródio, platina ou paládio, para serem empregados em reações químicas específicas, tais como hidrogenação, hidroformilação ou oxidação de alquenos e álcoois.

A presente invenção, que compreende o processo de preparo de partículas magnéticas recobertas por carbono, pode ser melhor entendida através dos seguintes exemplos:

Exemplo 1 - Em um reator (tubo de quartzo inserido dentro de um forno tubular horizontal), hematita sintética Fe_2O_3 foi aquecida em fluxo de metano com aquecimento entre 600 e 950°C a 5°Cmin^{-1}. Do forno, a mistura de gases foi direcionada, através de um amostrador com temporizador (configurado para fazer uma injeção a cada 3 minutos), a um aparelho de cromatografia gasosa com um detector de ionização por chama (FID). Este cromatógrafo foi utilizado para separar e monitorar a fonte de carbono e os produtos de reação. Resultados de DRX, Mossbauer, TG/DTA, Análise Elementar (CHN), TPR, BET, MEV e MET mostraram que o metano reduz o óxido de ferro produzindo magnetita (73 a 93%), wustita (9 a 77%) recoberta por uma camada de carbono (1 a 4%). A Figura 1 mostra os teores das fases de ferro formadas em diferentes condições de reação obtidas por espectroscopia Mössbauer. Estes materiais quando dispersos em água apresentaram grande quantidade de partículas menores que 200 nm em suspensão (Figura 2).

Exemplo 2 - Em um reator (tubo de quartzo inserido dentro de um forno tubular horizontal), hematita sintética foi aquecida em fluxo de vapor de etanol em nitrogênio (usado como gás de arraste) a temperaturas entre 350 e 950°C a 5°Cmin^{-1}. Resultados de DRX, Mossbauer, TG/DTA, Análise Elementar (CHN), TPR, BET, MEV e MET mostraram que o etanol reduz a hematita formando uma mistura contendo magnetita (40 a 59%), wustita (0 a 34%), ferro metálico (7 a 81%), carbeto de ferro (17 a 65%) recoberto por carbono (3 a 71%). A Figura 3 mostra os teores das fases de ferro formadas em diferentes condições de reação obtidas por espectroscopia Mössbauer. Medidas de difração de raios x e espectroscopia vibracional Raman indicaram a presença de material carbonáceo na forma de grafite e carbono amorfo. A Figura 4 mostra imagens

obtidas por microscopia eletrônica de varredura e de transmissão de partículas magnéticas com diâmetros menores que 200 nm recobertas por carbono na extremidade de tubos formados por carbono.

Exemplo 3 - Em um reator (tubo de quartzo inserido dentro de um forno tubular horizontal), hematita sintética foi aquecida em fluxo de vapor de tolueno em nitrogênio (usado como gás de arraste) a temperatura de 900°C a 5°Cmin^{-1}. Resultados de DRX, Mossbauer, TG/DTA, Análise Elementar (CHN), TPR, BET, MEV e MET mostraram que o material obtido é formado por ferro metálico (52%) e carbeto de ferro (16%) recoberto por carbono (32%).

Exemplo 4 - Em um reator (tubo de quartzo inserido dentro de um forno tubular horizontal), magnetita sintética foi colocada na presença de etanol em nitrogênio (usado como gás de arraste) e aquecida a 900°C a 5°Cmin^{-1}. Resultados de DRX, Mossbauer, TG/DTA, Análise Elementar (CHN), TPR, BET, MEV e MET mostraram que o material obtido é formado por ferro metálico (54%), carbeto de ferro (21%) e carbono (25%), conforme mostra Figura 5.

Exemplo 5 - Em um reator (tubo de quartzo inserido dentro de um forno tubular horizontal), maghemita sintética foi colocada na presença de etanol em nitrogênio (usado como gás de arraste) e aquecida a 900°C a 5°Cmin^{-1}. Resultados de DRX, Mossbauer, TG/DTA, Análise Elementar (CHN), TPR, BET, MEV e MET mostraram que o material obtido é formado por ferro metálico (21%), carbeto de ferro (69%) e carbono (10%), conforme mostra Figura 5.

Exemplo 6 - Em um reator (tubo de quartzo inserido dentro de um forno tubular horizontal), goetita sintética foi colocada na presença de etanol em nitrogênio (usado como gás de arraste) e aquecida a 900°C a 5°Cmin^{-1}. Resultados de DRX, Mossbauer, TG/DTA, Análise Elementar (CHN), TPR, BET, MEV e MET mostraram que o material obtido é formado por ferro metálico (56%), carbeto de ferro (30%) e carbono (14%), conforme mostra Figura 5.

Exemplo 7 - Em um reator (tubo de quartzo inserido dentro de um forno tubular horizontal), o rejeito lama vermelha foi colocado na presença de etanol em

nitrogênio (usado como gás de arraste) e aquecido em diferentes temperaturas entre 500 e 950°C a 5°Cmin^{-1}. Resultados de DRX, Mossbauer, TG/DTA, Análise Elementar (CHN), TPR, BET, MEV e MET mostraram que o material obtido é formado por fases como magnetita, goetita, wustita, ferro metálico, carbeto de ferro, além de CaO e SiO_2 e carbono (5 a 56%). Os teores das fases de ferro formadas são mostrados na Figura 6.

Exemplo 8 - Os materiais preparados nos Exemplos 1 a 7 foram dispersos em água e feita a separação da fração nanoparticulada/micro-macroparticulada após certo tempo de decantação. Para isto, o perfil da deposição destas partículas em água foi acompanhado pela medida da transmitância do material disperso em função do tempo, utilizando um espectrômetro UV-vis. Alíquotas da dispersão aquosa dos materiais que permanecem em suspensão foram coletadas e analisadas por MEV. O aspecto das partículas nanoparticuladas e um histograma da distribuição de tamanho dessas partículas para o material produzido no Exemplo 1 são mostrados na Figura 2.

Exemplo 9 - Aplicação dos materiais produzidos como adsorventes. Os materiais produzidos a partir da reação entre hematita e metano foram testados como adsorventes magnéticos de compostos aromáticos, i.e. BTX (benzeno, tolueno e xileno) e clorobenzeno (CIB), mostrando capacidades de adsorção da ordem de 6-15 mg/g. Para estes testes de adsorção, o material foi adicionado a uma solução aquosa contendo 50 ppm de clorobenzeno, e deixados em repouso por um dia. Os valores de absorvância foram então medidos utilizando um espectrômetro UV-vis.

Exemplo 10 - Aplicação dos materiais produzidos como suporte de catalisadores. Reações de hidrogenodescloração foram realizadas com Pd suportado nos materiais produzidos no Exemplo 1 e mostraram grande conversão de clorobenzeno em benzeno, mesmo após o terceiro uso do material (23-21 $mmol_{CIB}/mmol_{Pd}$). Para os testes catalíticos, Pd foi impregnado a partir do sal cloreto em água. EM seguida o material foi seco e reduzido com hidrogênio a 400°C.

Exemplo 11 - Aplicação dos materiais produzidos como suporte de catalisadores. Os materiais produzidos a partir da reação entre hematita e etanol (Exemplo 2) foram testados como suporte de catalisadores de Pd em reações de hidrogenodescloração de clorobenzeno (ClB) e mostraram grande conversão de clorobenzeno em benzeno (18 mmolClB/mmolPd no primeiro e segundo uso).

REIVINDICAÇÕES

1. **Processo de Obtenção de Partículas Magnéticas Recobertas por Carbono**, caracterizado pela obtenção das referidas partículas a partir do recobrimento de partículas de materiais à base de ferro com carbono provindo de diferentes fontes orgânicas aquecidas.

2. **Processo de Obtenção de Partículas Magnéticas Recobertas por Carbono**, de acordo com a reivindicação 1, caracterizado pelo uso de óxidos de ferro de origem sintética como hematita (α-Fe_2O_3), magnetita (Fe_3O_4), maghemita (γ-Fe_2O_3) e goetita (α-FeOOH).

3. **Processo de Obtenção de Partículas Magnéticas Recobertas por Carbono**, de acordo com a reivindicação 1, caracterizado pelo uso de óxidos de ferro de origem natural como hematita (α-Fe_2O_3), magnetita (Fe_3O_4), maghemita (γ-Fe_2O_3), goetita (α-FeOOH), itabirito e outros minerais contendo ferro tais como serpentinito.

4. **Processo de Obtenção de Partículas Magnéticas Recobertas por Carbono**, de acordo com a reivindicação 1, caracterizado pelo uso de qualquer rejeito industrial rico em óxidos de ferro como a lama vermelha, rejeitos de siderurgia, rejeitos de aciaria, não limitado.

5. **Processo de Obtenção de Partículas Magnéticas Recobertas por Carbono**, de acordo com a reivindicação 1, caracterizado pela fontes de carbono poderem ser hidrocarbonetos alifáticos e aromáticos como fonte de carbono como metano, etano, propano, butano, benzeno, tolueno, xileno, não limitado.

6. **Processo de Obtenção de Partículas Magnéticas Recobertas por Carbono**, de acordo com a reivindicação 1, caracterizado pelo uso de álcoois como fonte de carbono, como metanol, etanol, propanol, butanol, não limitado.

7. **Processo de Obtenção de Partículas Magnéticas Recobertas por Carbono**, caracterizado pelas partículas obtidas estarem compreendidas na faixa que pode variar de dimensões micro até nanométricas.

8. **Processo de Obtenção de Partículas Magnéticas Recobertas por Carbono**, de acordo com a reivindicação 7, caracterizado pela separação da fração nanométrica pela suspensão em um meio fluído que pode ser água ou um solvente orgânico.

9. **Processo de Obtenção de Partículas Magnéticas Recobertas por Carbono**, caracterizado pelo uso destes materiais para a remoção de contaminantes orgânicos de água, tais como contaminantes aromáticos, alifáticos, organoclorados, corantes, não limitado.

10. **Processo de Obtenção de Partículas Magnéticas Recobertas por Carbono**, caracterizado pelo uso destes materiais como suporte de catalisadores de metais nobres.

FIGURAS

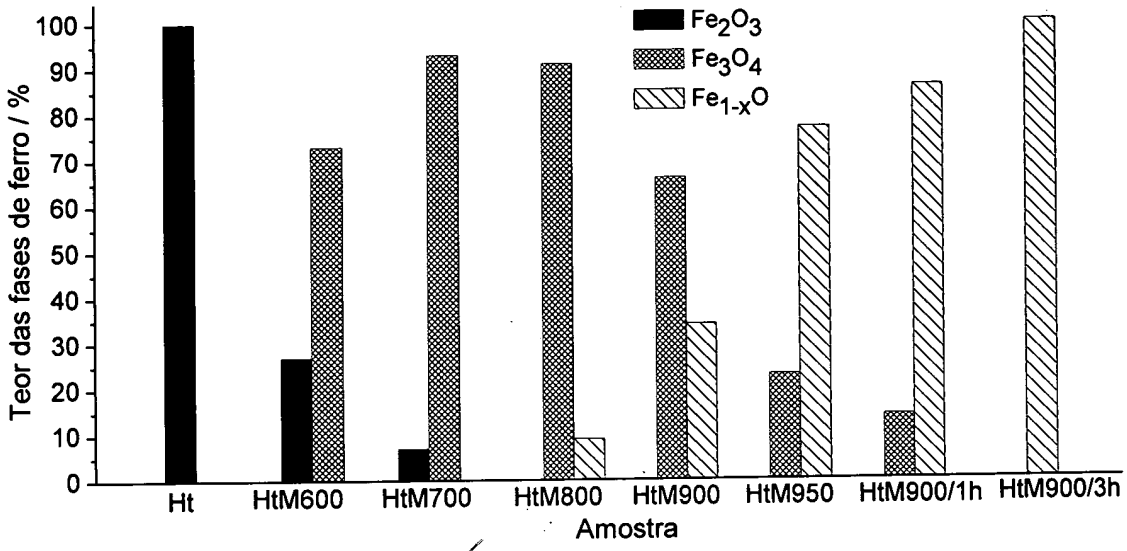

Figura 1

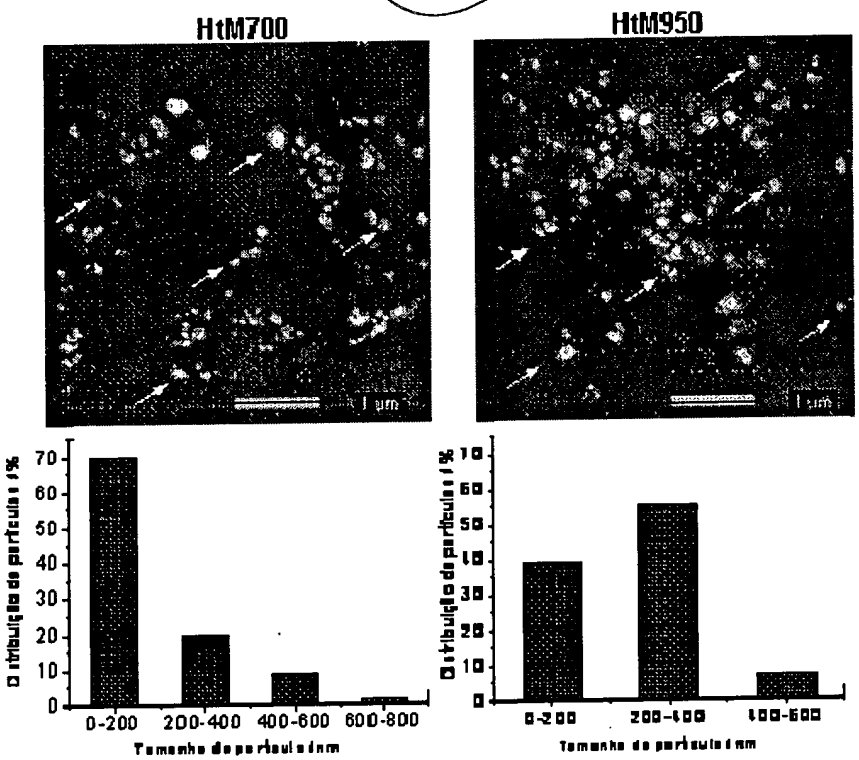

Figura 2

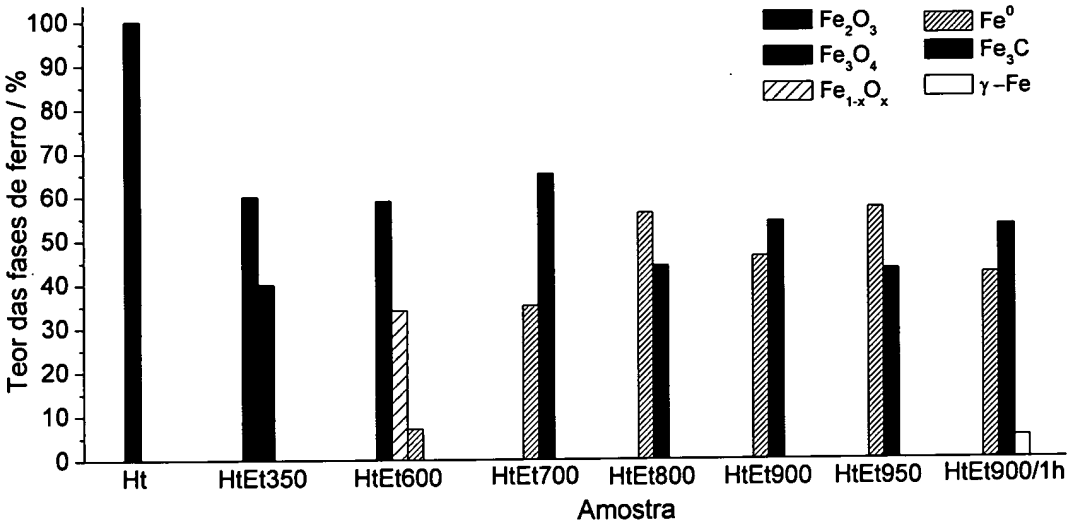

Figura 3

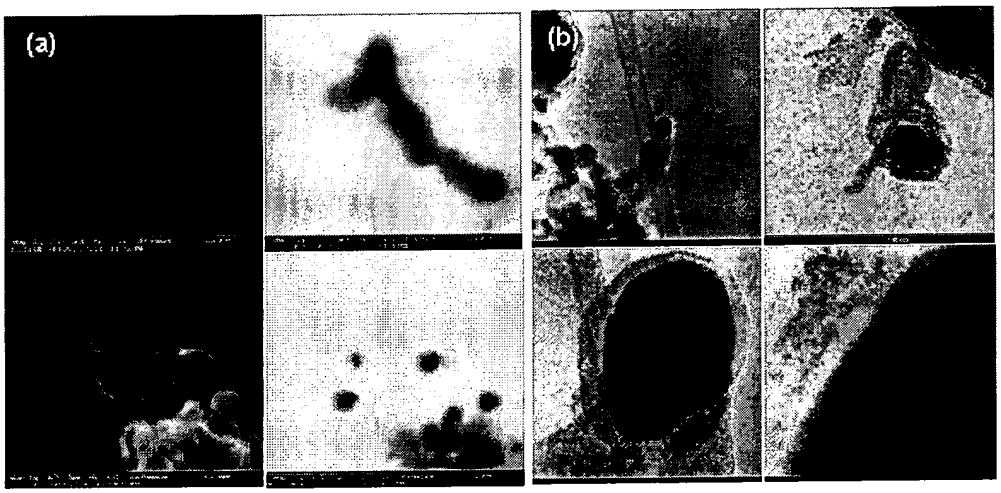

Figura 4

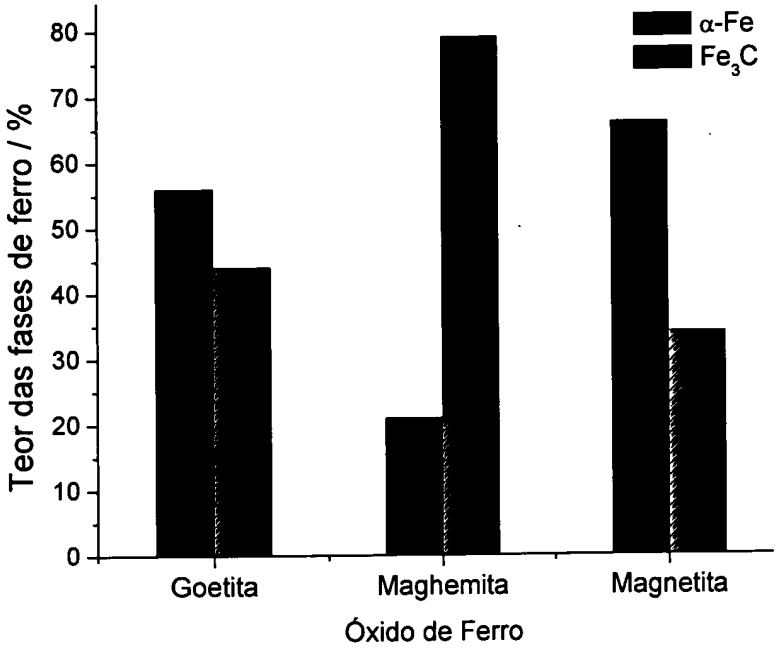

Figura 5

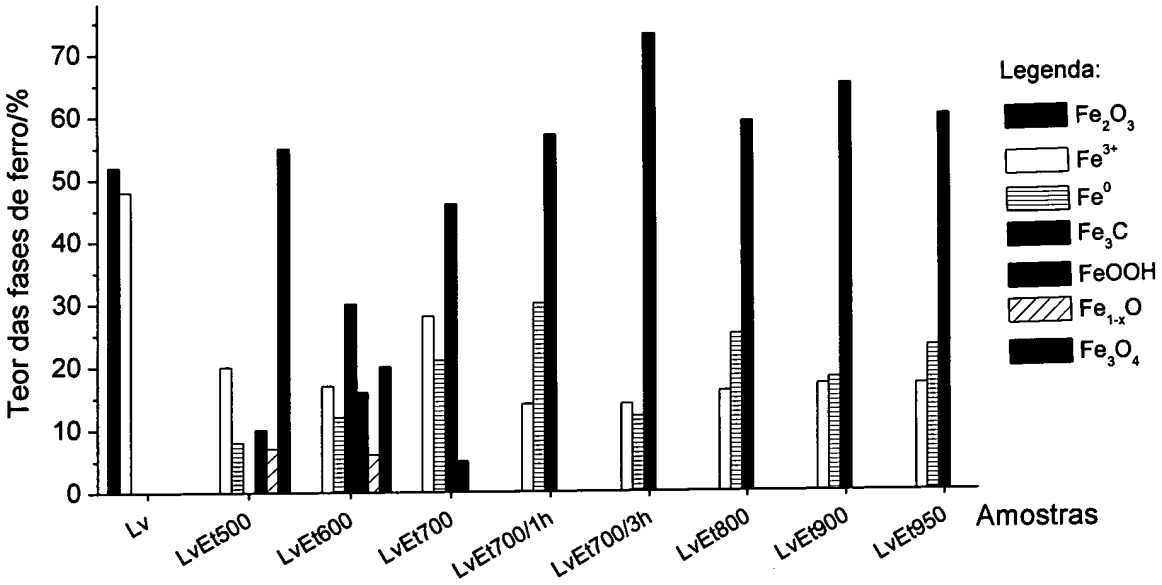

Figura 6

PI0904095-6

RESUMO

Processo de Obtenção de Partículas Magnéticas Recobertas por Carbono

A presente invenção descreve um processo para a produção de partículas magnéticas recobertas por carbono para serem utilizadas em aplicações tecnológicas. O caráter inovador desta invenção está na simplicidade e no baixo custo do processo que permite utilizar diversas fontes de ferro, tais como de origem sintética (α-Fe_2O_3, Fe_3O_4 e FeOOH), natural (minérios) ou rejeitos industriais (lama vermelha, rejeito de aciaria, rejeitos siderúrgicos). O recobrimento de carbono é realizado através de um processo de etapa única que envolve a redução dos óxidos de ferro para formar o núcleo magnético e deposição de carbono a partir de diferentes tipos de compostos orgânicos que também são insumos disponíveis e de baixo custo tais como metano e etanol.

ADVANCED FUNCTIONAL MATERIALS

FULL PAPER

DOI: 10.1002/adfm.200801386

Carbon Coated Fe_3O_4 Nanospindles as a Superior Anode Material for Lithium-Ion Batteries**

By *Wei-Ming Zhang, Xing-Long Wu, Jin-Song Hu, Yu-Guo Guo,** and *Li-Jun Wan**

Carbon-coated Fe_3O_4 nanospindles are synthesized by partial reduction of monodispersed hematite nanospindles with carbon coatings, and investigated with scanning electron microscopy, transmission electron microscopy, X-ray diffraction, and electrochemical experiments. The Fe_3O_4–C nanospindles show high reversible capacity (~745 mA h g^{-1} at C/5 and ~600 mA h g^{-1} at C/2), high coulombic efficiency in the first cycle, as well as significantly enhanced cycling performance and high rate capability compared with bare hematite spindles and commercial magnetite particles. The improvements can be attributed to the uniform and continuous carbon coating layers, which have several functions, including: i) maintaining the integrity of particles, ii) increasing the electronic conductivity of electrodes leading to the formation of uniform and thin solid electrolyte interphase (SEI) films on the surface, and iii) stabilizing the as-formed SEI films. The results give clear evidence of the utility of carbon coatings to improve the electrochemical performance of nanostructured transition metal oxides as superior anode materials for lithium-ion batteries.

1. Introduction

Rechargeable lithium-ion batteries have been the most utilized batteries in the portable electronic market for many years. They have the highest energy density available from existing rechargeable battery techniques, but their performance still lies behind the demands of the consumer. New electrode materials with high specific capacities are necessary to meet these demands. Recently, transition metal oxides have shown desirable properties, such as high theoretical capacity (~500–1000 mA h g^{-1}, compared with ~372 mA h g^{-1} for conventional graphite), based on a novel conversion mechanism,[1] making them promising anode materials for high performance lithium-ion batteries.[1–10] However, most of the transition metal oxides usually suffer from the problem of poor electronic conduction, and hence need to be modified by admixing electronically conductive phases.[11] There are very few transition metal oxides such as Fe_3O_4 and RuO_2 with high electronic conductivities.[6–8,12,13] As Fe_3O_4 has advantages over RuO_2 in terms of low cost and environmental benignity, extensive research work has focused on it recently.[6–8] Another challenge in using transition metal oxides as anode materials is their poor cycling performance; the electrodes cannot maintain their integrity over several discharge/charge cycles. It has been widely demonstrated that this problem can be partly solved in nanostructured electrode materials because of better accommodation of the strains of Li insertion/extraction than in micrometer-scale materials.[1,14–19] However, the high surface area of nanostructured electrode materials raises the risk of secondary reactions involving electrolyte decomposition between electrode and electrolyte, which causes a high level of irreversibility (i.e., low columbic efficiency) and poor life cycle, and the formation of thick solid electrolyte interphase (SEI) films on the electrode surface, which consume much of the Li supplied by the cathodes.[12] Furthermore, it has been found in many nanostructured transition metal oxides that thick SEI films formed during Li uptake may disappear completely, catalyzed by transition metal upon Li extraction, which leads to capacity fading and safety problems.[1,9,13,20,21] Therefore, surface modifications must be considered for nanostructured transition metal oxides.

Carbon coating is one of the most widely used surface modification techniques for cathode materials (e.g., $LiFePO_4$), because carbon coating layers can significantly enhance the electronic conductivity of electrode materials, which results in improved rate performance.[22–24] In fact, carbon materials are very stable anode materials in lithium-ion batteries due to the small volume change during Li insertion/extraction. The SEI films on carbon surface are also relatively stable.[21,25,26] Therefore, carbon coatings should be also used for anode materials since they may serve as perfect barriers to protect the

[*] Prof. L.-J. Wan, Prof. Y.-G. Guo, W.-M. Zhang, X.-L. Wu, Dr. J.-S. Hu
Key Laboratory of Molecular Nanostructure and Nanotechnology
Institute of Chemistry, Chinese Academy of Sciences (CAS)
Beijing 100190 (PR China)
E-mail: wanlijun@iccas.ac.cn
Prof. L.-J. Wan, Prof. Y.-G. Guo, W.-M. Zhang, X.-L. Wu, Dr. J.-S. Hu
Beijing National Laboratory for Molecular Sciences (BNLMS)
Beijing 100190 (PR China)
E-mail: ygguo@iccas.ac.cn
W.-M. Zhang, X.-L. Wu
Graduate School of CAS
Beijing 100064 (PR China)

[**] This work is supported by the National Natural Science Foundation of China (Grant nos. 20603041, 50730005, and 20701038), National Key Project on Basic Research (Grant nos. 2006CB806100 and 2009CB930400), and the Chinese Academy of Sciences. Supporting Information is available online from Wiley InterScience or from the author.

© 2008 WILEY-VCH Verlag GmbH & Co. KGaA, Weinheim

inner active materials and maintain their high capacities.[26–29] In this Full Paper, we successfully synthesize a superior anode material for lithium-ion batteries by introducing carbon coatings on the surface of iron oxide nanospindles. It is found that the carbon coating layers not only enhance the electronic conductivity of electrode materials, but also lead to stabilized SEI films. As a result, the as-prepared carbon coated Fe_3O_4 nanospindles exhibit very high specific capacity (~749 mA h g^{-1} at C/5 and ~600 mA h g^{-1} at C/2), significantly improved cycling performance, and high rate performance compared with commercial magnetite particles and bare hematite nanospindles.

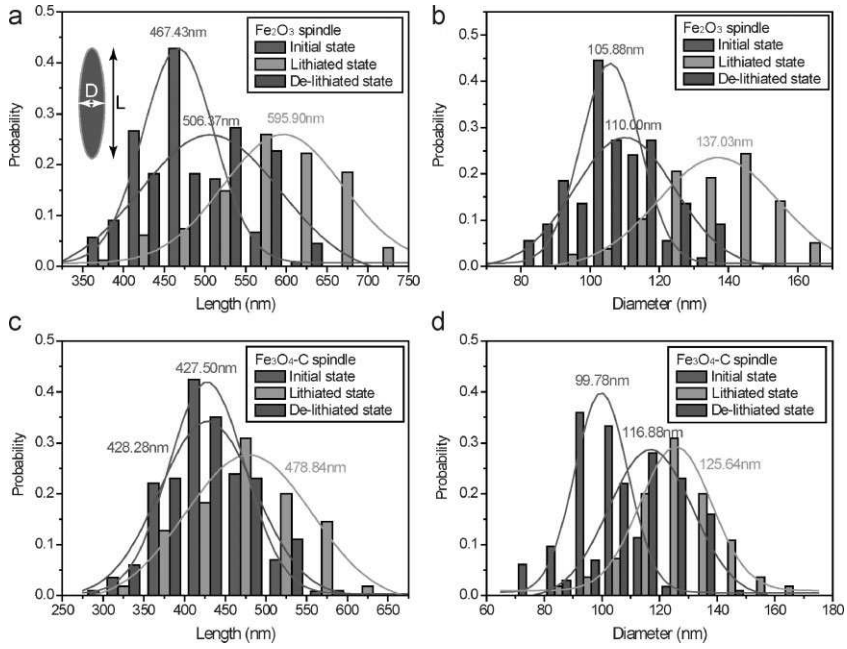

Figure 2. The a) length and b) diameter distributions of bare α-Fe_2O_3 nanospindles in initial, lithiated and de-lithiated state; the c) length and d) diameter distributions of Fe_3O_4–C nanospindles in initial, lithiated, and de-lithiated state. The inset in the left top picture shows the meaning of length and diameter for a spindle.

2. Results and Discussion

The carbon coated magnetite nanospindles were prepared by in situ partial reduction of hematite spindles with carbon coatings. First, the monodispersed spindle hematite particles were synthesized by forced hydrolysis of ferric chloride solutions with small additions of phosphate ions at elevated temperatures.[30] Figure 1a shows the scanning electron microscopy (SEM) image of as-synthesized hematite spindles. All particles are spindles alike, composed of tiny crystals. They have a mean particle length of about 470 nm and a diameter of about 106 nm. The detailed statistical distributions of the particle length and diameter are shown in Figure 2a and b, respectively.

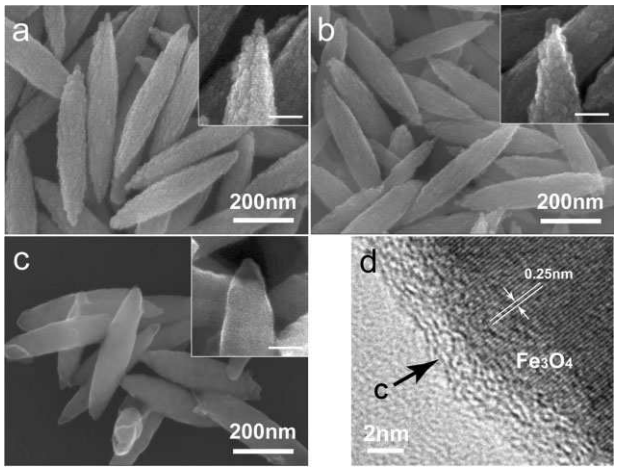

Figure 1. a) SEM image of the as-synthesized hematite spindles. b) SEM image of the carbon precursor coated hematite spindles. c) SEM image of the carbon coated Fe_3O_4 spindles (Fe_3O_4–C composites). d) high-resolution transmission electron microscopy (TEM) image of the Fe_3O_4–C composites. The insets are close views of corresponding samples, all unmarked scale bars are 50 nm.

Figure 3a shows the power X-ray diffraction (XRD) pattern of the same sample, in which all peaks are in good agreement with α-Fe_2O_3 (JCPDS no. 89-8103, $a = b = 5.020$ Å, $c = 13.719$ Å). Both the morphology and structure are in agreement with those reported in the literature.[30]

Secondly, the carbon precursor layers were coated on the outer surface of the hematite spindles by pyrolysis of glucose under hydrothermal conditions.[29,31] Figure 1b shows the SEM micrograph of the carbon-precursor-coated hematite spindles; it can be seen that there is no significant change in morphology, indicating uniform carbon coatings. Finally, the products were dried and heat-treated at 600 °C for about 12 h under N_2

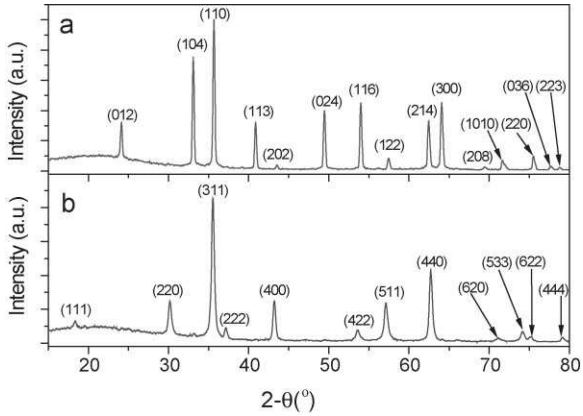

Figure 3. XRD patterns of a) hematite spindles, and b) Fe_3O_4–C composites. They are identified as rhomb-centered α-Fe_2O_3 (JCPDS no. 89-8103) and face-centered Fe_3O_4 (JCPDS no. 65-3107), respectively.

 © 2008 WILEY-VCH Verlag GmbH & Co. KGaA, Weinheim

atmosphere to carbonize the carbon precursor layers. At the same time, the inner hematite spindles were partially reduced to magnetite by the outer carbon layers, hence leading to the final Fe_3O_4–C nanocomposites. Figure 1c shows the SEM micrograph of the final composites; they have much smoother surfaces than the precursor. The mean length and diameter of the resultant Fe_3O_4–C spindles were about 428 and 100 nm, respectively (see Figure 2c and d for details). It can also be seen, from the inset in Figure 1c, that the composites have a small void space at the tips of the spindles. All evidence indicates that there is slight volume shrinkage during the heat-treatment process, which is likely to be due to the partial reduction process of α-Fe_2O_3. The high-resolution transmission electron microscopy (TEM) micrograph of the composite is shown in Figure 1d; both the outer carbon layer and the inner magnetite core are visible. The carbon layer, which has a thickness of ~2–10 nm, is uniform and continuous. More detailed TEM micrographs of the carbon layers can be found in Figure S1 of the Supporting Information.

To clarify the structure of the composites, XRD experiments were carried out. Figure 3b shows the XRD pattern of the final Fe_3O_4–C spindles, which is in good agreement with face-centered Fe_3O_4 (JCPDS no. 65-3107, $a = b = c = 8.390$ Å). No obvious XRD peaks corresponding to graphite are found in the XRD pattern, which indicates the carbon coatings are not well crystallized. The γ-Fe_2O_3 particles have similar XRD patterns to Fe_3O_4, but they cannot exist at the heat-treatment temperature as they convert to α-Fe_2O_3 at about 400 °C. Therefore, the products can be identified with Fe_3O_4, which is further confirmed by the color change from brown to totally black during heat treatment and the strong ferromagnetism of the final black products. It can be concluded that the α-Fe_2O_3 spindles were fully converted to Fe_3O_4 because the peaks unique for Fe_2O_3 (including the peaks at 24.1, 33.08, and 40.86° in Figure 3a), disappeared completely in Figure 3b. Note that the slightly broadened XRD peaks occurring after the partial reduction process are ascribed to the crystal size change from about 40 nm in hematite spindles to 30 nm in magnetite spindles, indicating that both of the spindles are composed of fine crystalline particles.

In order to investigate the pore structure of the α-Fe_2O_3 and Fe_3O_4–C spindles, a nitrogen isothermal adsorption technique was used. The results are shown in Figure S2 of the Supporting Information. The Brunauer–Emmett–Teller (BET) surface areas of the α-Fe_2O_3 and Fe_3O_4–C spindles are 14.6 and 35.1 m^2 g^{-1}, respectively. The Barrett–Joyner–Halenda (BJH) pore size distribution indicates that, besides the big interspaced pores among particles, the composite has mesopores of about 3.8 nm compared with bare Fe_2O_3, which may also come from the crystal volume shrinkage during the partial reducing process. They are helpful for buffering the volume expansion during lithium insertion, which may contribute to a better cycling performance. Furthermore, inductively coupled plasma-optical emission spectroscopy was used to reveal the precise chemical composition of the final composites. The results showed that the composites have a chemical composition of 78.5 wt% Fe_3O_4 and 21.5 wt% carbon, which leads to a theoretical specific capacity of 805 mA h g^{-1} for the Fe_3O_4–C spindles when being used as anode material in lithium-ion batteries. Note that we include the mass of carbon coating layers when calculating the specific capacity of Fe_3O_4–C composite in the context.

In order to test the applicability of the new composites in lithium-ion batteries, the electrochemical properties with respect to Li insertion/extraction were investigated. The electrochemical properties of bare α-Fe_2O_3 spindles and commercial Fe_3O_4 particles (Alfa Aesar, ~300 nm in diameter) were also investigated for comparison. Although the commercial magnetite particles and the Fe_3O_4-C spindles have different morphology, they have comparable particle size. The SEM images of the commercial Fe_3O_4 particles, α-Fe_2O_3 spindles, and Fe_3O_4–C composites on copper foil electrodes are shown in Figure S3, S4a, and S4d of the Supporting Information, respectively. The first five discharge/charge cycles were tested at a relatively low current rate of C/5 (8 lithium per Fe_3O_4 in 5 h), and the corresponding discharge/charge voltage profiles are shown in Figure 4. In the first discharge curve, that of the bare α-Fe_2O_3 (Fig. 4a), there are two obvious potential plateaus at about 1.6 and 0.8 V versus Li^+/Li, which are similar to those reported for Fe_2O_3.[4,32] In the cases of the commercial Fe_3O_4 (Fig. 4b) and the Fe_3O_4–C composites (Fig. 4c), the first discharge curves are very similar, with only one potential plateau at about 0.8 V versus Li^+/Li, which are close to that described in the literature for Fe_3O_4 anodes.[7,8] The specific charge capacities of both the commercial Fe_3O_4 particles and the bare α-Fe_2O_3 quickly fade, and show poor cycling performance, while the Fe_3O_4–C composite shows much better performance. The first specific charge capacity of Fe_3O_4–C composite is as high as 749 mA h g^{-1}, approaching

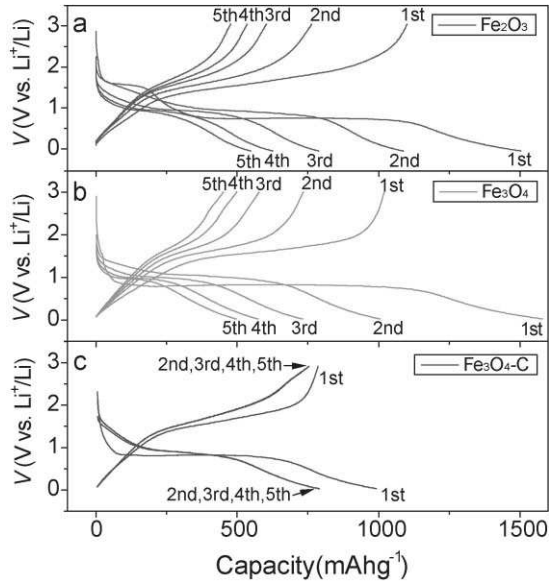

Figure 4. The discharge/charge profiles of a) bare hematite spindles, b) commercial magnetite particles, and c) Fe_3O_4–C composites, at a current rate of C/5.

© 2008 WILEY-VCH Verlag GmbH & Co. KGaA, Weinheim

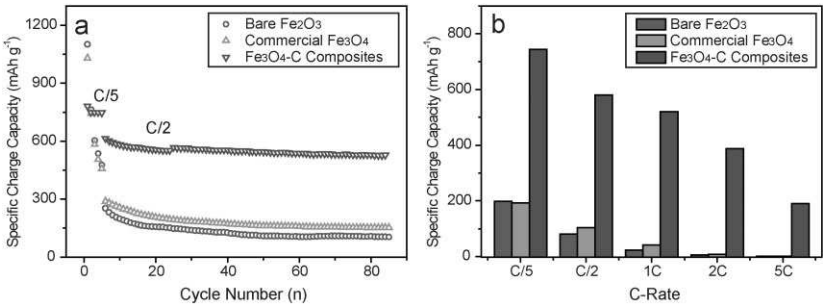

Figure 5. a) Cycle performance and b) rate performance of the bare α-Fe_2O_3 spindles, commercial Fe_3O_4 particles and Fe_3O_4–C composites.

~93% of its theoretical specific capacity (805 mA h g^{-1}). The capacity of the composite remains unchanged through the subsequent four discharge/charge cycles, as shown in Figure 4c, in which the discharge/charge curves of these cycles overlap. The initial coulombic efficiency of the Fe_3O_4–C composite is ~80%, which is significantly higher than ~70% of the bare α-Fe_2O_3 spindles and ~65% of the commercial Fe_3O_4 particles, showing a remarkable decrease of the irreversible capacity loss. The subsequent 80 cycles were tested at a relatively high current rate of C/2. The results from these cycles are shown in Figure 5a. It was found that the capacity of the bare α-Fe_2O_3 and the commercial Fe_3O_4 fade to 250 and 300 mAh g^{-1} immediately and then gradually decreased to 105 and 152 mA h g^{-1}, respectively. The capacity of Fe_3O_4–C composites also decrease to about 600 mA h g^{-1}, but the capacity remained 530 mA h g^{-1} even after another 80 discharge/charge cycles, which is almost 5 times of that of the bare α-Fe_2O_3 spindles and 3.5 times of that of the commercial Fe_3O_4 particles.

In addition to the much improved cycling performance, the Fe_3O_4–C composites also show significantly enhanced high rate performance compared with the bare α-Fe_2O_3 spindles and the commercial Fe_3O_4 particles (Fig. 5b). At a high rate of 5 C (discharge/charge of all active materials within 12 min, i.e., 4620 mA g^{-1}), the specific charge capacity of Fe_3O_4–C composites is still 190 mA h g^{-1}, whereas α-Fe_2O_3 spindles and commercial Fe_3O_4 particles nearly have no capacities at this condition. The results indicate that the improvement in electrochemical performance, in terms of cycling performance and rate performance, should not be attributed to the magnetite itself or the spindle type morphology, but the carbon coating layers outside the magnetite.

In order to well understand the effects of the carbon coatings on the electrochemical properties of Fe_3O_4 nanospindles, the intermediate states of the Fe_3O_4–C composites during Li insertion/extraction were investigated in detail. The anode materials were investigated on the electrodes by SEM. Figure S4 of the Supporting Information shows the SEM images of the electrodes of bare α-Fe_2O_3 spindles and Fe_3O_4–C composites in the initial, lithiated and de-lithiated state. Since the Fe_3O_4–C composites have continuous carbon coatings (see Figure S1 of the Supporting Information), they can form a more efficient electron conductive network, which is helpful for both cycle performance and rate performance.[11] In addition, nearly all Fe_3O_4–C spindles are unbroken on the battery electrode, indicating the composites are stable and strong enough to withstand the casting and pressing processes necessary for battery fabrication. The α-Fe_2O_3 and Fe_3O_4–C anode materials were further investigated by TEM after several discharge/charge cycles. Figure 6 shows the TEM images of the α-Fe_2O_3 and Fe_3O_4–C spindles in both the fully lithiated (discharge) and fully de-lithiated (charge) states. The spindle-like morphology of both materials remained unchanged during the discharge/charge cycles in both states. For the Fe_3O_4–C composites, as shown in Figure 6a and b, the total thickness of the outer carbon layer plus the SEI film is relatively thin, which is about 10 nm in fully lithiated and de-lithiated states. Furthermore, the thickness of the SEI films has no significant change during the insertion/extraction of lithium. However, the SEI films on the bare α-Fe_2O_3 spindles are much more thick and unstable, as shown in Figure 6c and d, which can be 20–50 nm in fully lithiated state whiles 0–20 nm in de-lithiated state. Similar reports have been found on other bare transition metal oxides such as RuO_2[12], Cr_2O_3[21], and Co_3O_4[26]. To further confirm the results, the length and the diameter distributions of both spindle-like anode materials in the initial, lithiated and de-lithiated states were analyzed based on the SEM images. Note that we include the lengths and diameters of the SEI films when analyzing the data. The statistical results are shown in Figure 2. All data in this figure come from corresponding SEM images similar to Figure S4 of the Supporting Information but with a magnification of 20 000×, and the sample capacities are about 100 in all statistics. From the results, we can see that the length change and diameter change of the bare α-Fe_2O_3 spindles between the

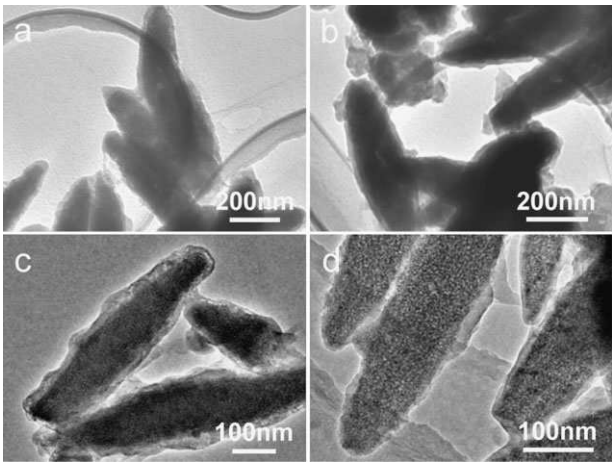

Figure 6. a) TEM images of the Fe_3O_4–C composites in a fully lithiated state. b) Fe_3O_4–C composites in a fully de-lithiated state. c) Bare α-Fe_2O_3 composites in a fully lithiated state. d) Bare α-Fe_2O_3 composites in a fully de-lithiated state after 3 discharge/charge cycles at a rate of C/5.

© 2008 WILEY-VCH Verlag GmbH & Co. KGaA, Weinheim

lithiated and de-lithiated states is about 90 nm (596 nm – 506 nm) and 27 nm (137 nm – 110 nm), respectively. However, in the case of Fe_3O_4–C spindles, the length change is only about 51 nm (479 nm – 428 nm), and the diameter change is only 9 nm (126 nm – 117 nm). This means that the SEI films are much more stable on the composite surface, namely under much smaller volume changes. The results indicate that the outer carbon layer can protect the inner active material as well as restrain the formation/decomposition of the SEI films. Note that even in the absence of carbon black, the Fe_3O_4–C itself still performs better than the bare α-Fe_2O_3 and the commercial Fe_3O_4 without carbon black. These results indicate that it is the outer carbon layer that contributes most to the great enhancement of both the cycle performance and the rate performance.

3. Conclusions

In summary, we synthesized new carbon coated Fe_3O_4 spindles with length of about 500 nm and an axis ratio of about 4. It was demonstrated that outer carbon layers with uniform and continuous features improve the electrochemical performance in several ways, including: i) maintaining the integrity of particles, ii) increasing the electronic conductivity of electrodes leading to the formation of uniform and thin SEI films on the surface, and iii) stabilizing the as-formed SEI films. As a result, a Fe_3O_4–C composite is a promising anode material for highly efficient lithium-ion batteries with high reversible capacity ($\sim$745 mA h g^{-1} at C/5 and $\sim$600 mA h g^{-1} at C/2), high coulombic efficiency in the first cycle, and significantly enhanced cycling performance and high rate capability compared with bare hematite spindles and commercial magnetite particles. The results presented here give clear evidence of the ability of carbon coatings to improve the electrochemical performance of nanostructured transition metal oxides as superior anode materials for lithium-ion batteries. We believe that the strategy will pave the way for the practical application of nanostructured transition metal oxides and, hence, make possibly the next generation of high-energy-density lithium-ion batteries.

4. Experimental

Preparation of Hematite Nanospindles: All reagents below were received from Beijing Chemicals Co. (Beijing, China) and used without further purification. A 75 mL mix solution containing 0.02 M $FeCl_3 \cdot 6H_2O$ and 0.45 mM NaH_2PO_4 in deionized (DI) water was transferred to a 100 mL teflon autoclave, and then heated at 105 °C in an electric oven for 48 h. After the autoclave cooled down, the monodispersed hematite particles were centrifuged and washed with DI water.

Preparation of Carbon Coated Fe_3O_4 Nanospindles: A 300 mg hematite particles was dispersed in 5 mL DI water by ultrasonication to form a suspension. 600 mg glucose ($C_6H_{12}O_6 \cdot 3H_2O$) was dissolved in another 15 mL DI water, and the former suspension and another 10 mL of ethanol were added to the solution under gentle stir. The resulting suspension was transferred to a 40 mL Teflon autoclave, which was then heated at 190 °C in an electric oven for 12–15 h. The carbon-precursor-coated hematite particles were harvested by centrifugation and washed with DI water, then dried at 110 °C in an oven. The resulting sample was heated in a quartz tube at a rate of 6 °C min^{-1} to 600 °C in N_2 atmosphere. The temperature was kept constant for another 12 h before the tube was allowed to cool down to room temperature.

Inductively Coupled Plasma-Optical Emission Spectroscopy Measurement: 13.3 mg dried Fe_3O_4–C composites were completely dissolved in 5 mL concentrated nitric acid by heating, and the resulting yellow solution was diluted to 1 000 mL with DI water. The resulting solution was analyzed by Optima 5300DV, and the concentration of the Fe element was 7.556 mg L^{-1}.

Characterization: The products were characterized by SEM (JEOL 6701F), TEM (TEM, JEM JEOL 2010 and 1011), XRD (Rigaku Dmax-rB diffractometer with CuKα radiation, k = 0.1542 nm, 40 kV, 100 mA). All SEM and TEM samples of active material in the lithiated/de-lithiated state were prepared in an argon-filled glove box, washed three times with dimethyl carbonate (DMC), and sealed in an argon-filled jar before characterization.

Electrochemical Characterization: Electrochemical experiments were performed using Swagelok-type cells. The working electrodes were prepared by mixing the α-Fe_2O_3 spindles, commercial Fe_3O_4 particles or Fe_3O_4–C composites, carbon black, and poly(vinyl difluoride) (PVDF) at a weight ratio of 70:15:15, and pasted on pure Cu foil. Glass fiber (GF/D) from Whatman was used as a separator. The electrolyte consists of a solution of 1 M $LiPF_6$ in ethylene carbonate (EC)/dimethyl carbonate (DMC)/diethyl carbonate (DEC) (1:1:1, in wt%) obtained from Ferro Corporation. Pure lithium foil was used as counter electrode. The discharge and charge measurements were carried on an Arbin BT2000 system. The cells were assembled in an argon-filled glove box.

Received: September 17, 2008
Published online: November 13, 2008

[1] P. Poizot, S. Laruelle, S. Grugeon, L. Dupont, J. M. Tarascon, *Nature* **2000**, *407*, 496.
[2] P. Poizot, S. Laruelle, S. Grugeon, L. Dupont, J. M. Tarascon, *J. Power Sources* **2001**, *97*, 235.
[3] P. Poizot, S. Laruelle, S. Grugeon, J. M. Tarascon, *J. Electrochem. Soc.* **2002**, *149*, A1212.
[4] J. Chen, L. Xu, W. Li, X. Gou, *Adv. Mater.* **2005**, *17*, 582.
[5] B. T. Hang, I. Watanabe, T. Doi, S. Okada, J. I. Yamaki, *J. Power Sources* **2006**, *161*, 1281.
[6] S. Ito, K. Nakaoka, A. Kawamura, K. Ui, K. Fujimoto, N. Koura, *J. Power Sources* **2005**, *146*, 319.
[7] S. Mitra, P. Poizot, A. Finke, J. M. Tarascon, *Adv. Funct. Mater.* **2006**, *16*, 2281.
[8] P. L. Taberna, S. Mitra, P. Poizot, P. Simon, J. M. Tarascon, *Nat. Mater.* **2006**, *5*, 567.
[9] A. Debart, L. Dupont, P. Poizot, J. B. Leriche, J. M. Tarascon, *J. Electrochem. Soc.* **2001**, *148*, A1266.
[10] Y. Yu, C. H. Chen, Y. Shi, *Adv. Mater.* **2007**, *19*, 993.
[11] Y.-G. Guo, Y. S. Hu, W. Sigle, J. Maier, *Adv. Mater.* **2007**, *19*, 2087.
[12] O. Delmer, P. Balaya, L. Kienle, J. Maier, *Adv. Mater.* **2008**, *20*, 501.
[13] P. Balaya, H. Li, L. Kienle, J. Maier, *Adv. Funct. Mater.* **2003**, *13*, 621.
[14] X. W. Lou, Y. Wang, C. L. Yuan, J. Y. Lee, L. A. Archer, *Adv. Mater.* **2006**, *18*, 2325.
[15] F. Jiao, P. G. Bruce, *Adv. Mater.* **2007**, *19*, 657.
[16] S. Grugeon, S. Laruelle, R. Herrera-Urbina, L. Dupont, P. Poizot, J. M. Tarascon, *J. Electrochem. Soc.* **2001**, *148*, A285.
[17] J. Maier, *Nat. Mater.* **2005**, *4*, 805.

© 2008 WILEY-VCH Verlag GmbH & Co. KGaA, Weinheim

[18] A.-M. Cao, J.-S. Hu, H.-P. Liang, L.-J. Wan, *Angew. Chem., Int. Ed.* **2005**, *44*, 4391.
[19] F. Cheng, Z. Tao, J. Liang, J. Chen, *Chem. Mater.* **2008**, *20*, 667.
[20] J. Jamnik, J. Maier, *Phys. Chem. Chem. Phys.* **2003**, *5*, 5215.
[21] J. Hu, H. Li, X. Huang, L. Chen, *Solid State Ionics* **2006**, *177*, 2791.
[22] R. Dominko, J. M. Goupil, M. Bele, M. Gaberscek, M. Remskar, D. Hanzel, J. Jamnik, *J. Electrochem. Soc.* **2005**, *152*, A858.
[23] Q. Cao, H. P. Zhang, G. J. Wang, Q. Xia, Y. P. Wu, H. Q. Wu, *Electrochem. Commun.* **2007**, *9*, 1228.
[24] Y.-S. Hu, Y.-G. Guo, R. Dominko, M. Gaberscek, J. Jamnik, J. Maier, *Adv. Mater.* **2007**, *19*, 1963.
[25] D. Aurbach, M. D. Levi, E. Levi, A. Schechter, *J. Phys. Chem. B* **1997**, *101*, 2195.
[26] S. A. Needham, G. X. Wang, K. Konstantinov, Y. Tournayre, Z. Lao, H. K. Liu, *Electrochem. Solid-State Lett.* **2006**, *9*, A315.
[27] G. Derrien, J. Hassoun, S. Panero, B. Scrosati, *Adv. Mater.* **2007**, *19*, 2336.
[28] G. Cui, Y. Hu, L. Zhi, D. Wu, I. Lieberwirth, J. Maier, K. Müllen, *Small* **2007**, *3*, 2066.
[29] W.-M. Zhang, J.-S. Hu, Y.-G. Guo, S.-F. Zheng, L.-S. Zhong, W.-G. Song, L.-J. Wan, *Adv. Mater.* **2008**, *20*, 1160.
[30] M. Ozaki, S. Kratohvil, E. Matijevic, *J. Colloid Interface Sci.* **1984**, *102*, 146.
[31] X.-M. Sun, Y.-D. Li, *Angew. Chem. Int. Ed.* **2004**, *43*, 597.
[32] D. Larcher, C. Masquelier, D. Bonnin, Y. Chabre, V. Masson, J. B. Leriche, J. M. Tarascon, *J. Electrochem. Soc.* **2003**, *150*, A133.

© 2008 WILEY-VCH Verlag GmbH & Co. KGaA, Weinheim

PERGAMON

Carbon 40 (2002) 2177–2183

CARBON

Activated carbon/iron oxide magnetic composites for the adsorption of contaminants in water

Luiz C.A. Oliveira[a], Rachel. V.R.A. Rios[a], José D. Fabris[a], V. Garg[c], Karim Sapag[b], Rochel M. Lago[a,*]

[a]*Departamento de Química, UFMG, Av. Antonio Carlos 6627, CEP 31270901, Belo Horizonte, MG, Brazil*
[b]*Lab. Cs. Superficie Medios Porosos, Univ. Nacional de San Luis, R. Chacabuco 917 (5700), Argentina*
[c]*Universidade Federal de Brasília, UNB, Brasília, DF, Brazil*

Received 28 November 2001; accepted 13 February 2002

Abstract

In this work the adsorption features of activated carbon and the magnetic properties of iron oxides were combined in a composite to produce magnetic adsorbents. These magnetic particles can be used as adsorbent for a wide range of contaminants in water and can subsequently be removed from the medium by a simple magnetic procedure. Activated carbon/iron oxide magnetic composites were prepared with weight ratios of 2:1, 1.5:1 and 1:1 and characterized by powder XRD, TG, magnetization measurements, chemical analyses, TPR, N_2 adsorption–desorption isotherms, Mössbauer spectroscopy and SEM. The results suggest that the main magnetic phase present is maghemite (γ-Fe_2O_3) with small amounts of magnetite (Fe_3O_4). Magnetization enhancement can be produced by treatment with H_2 at 600 °C to reduce maghemite to magnetite. N_2 adsorption measurements showed that the presence of iron oxides did not significantly affect the surface area or the pore structure of the activated carbon. The adsorption isotherms of volatile organic compounds such as chloroform, phenol, chlorobenzene and drimaren red dye from aqueous solution onto the composites also showed that the presence of iron oxide did not affect the adsorption capacity of the activated carbon.
© 2002 Published by Elsevier Science Ltd.

Keywords: A. Activated carbon; C. Adsorption; D. Magnetic properties, Surface areas

1. Introduction

The application of magnetic particle technology to solve environmental problems has received considerable attention in recent years. Magnetic particles can be used to adsorb contaminants from aqueous or gaseous effluents and, after adsorption, can be separated from the medium by a simple magnetic process. Examples of this technology are the use of magnetite particles to accelerate the coagulation of sewage [1], a magnetite-coated functionalized polymer such as a resin to remove radionuclides from milk [2], poly(oxy-2,6-dimethyl-1,4-phenylene) for the adsorption of organic dyes [3] and polymer-coated magnetic particles for oil spill remediation [4]. However, all these materials have the drawback of a small surface area or a small adsorption capacity, which limits their application. Moreover, the preparation of these magnetic materials requires several steps, and special chemicals and procedures. In this work, high surface area and high adsorption capacity magnetic composites based on activated carbon/iron oxide were prepared by a simple method and used for the removal of contaminants from aqueous effluents.

Activated carbons offer an attractive and inexpensive option for the removal of organic and inorganic contaminants from water [5,6]. Due to its high surface area and porous structure it can efficiently adsorb gases and compounds dispersed or dissolved in liquids [7–9]. The adsorption of several organic contaminants in water, such as pesticides, phenols and chlorophenols, has recently been

*Corresponding author. Tel.: +55-31-34995-719; fax: +55-31-34995-700.

E-mail address: rochel@dedalus.lcc.ufmg.br (R.M. Lago).

0008-6223/02/$ – see front matter © 2002 Published by Elsevier Science Ltd.
PII: S0008-6223(02)00076-3

reported [10–16]. Moreover, activated carbon can easily be functionalized and used as an efficient adsorbent for heavy metal cationic contaminants [17].

2. Experimental

The composites were prepared from a suspension of activated carbon (Aldrich Darco G60, 100 mesh, American Norit) in a 400 ml solution of $FeCl_3$ (7.8 g, 28 mmol) and $FeSO_4$ (3.9 g, 14 mmol) at 70 °C. NaOH solution (100 ml, 5 mol l^{-1}) was added dropwise to precipitate the iron oxides. The amount of activated carbon was adjusted in order to obtain activated carbon/iron oxide weight ratios of 1:1, 2:1 and 3:1. The obtained materials were dried in an oven at 100 °C for 3 h and characterized by powder XRD (Ni filtered Cu Kα, $\lambda = 1.5418$ Å), TG analysis and magnetization measurements carried out in a portable magnetometer with a fixed magnetic field of 0.3 T [18]. The samples were also analyzed chemically for Fe^{2+} and Fe^{3+}. Temperature programmed reduction (TPR) profiles, Mössbauer spectra (obtained with a $^{57}Co/Rh$ source at liquid N_2 temperature calibrated with α-Fe) and scanning electron microscopy (SEM) analyses were also used for characterization. The adsorption isotherms were obtained in batch equilibrium experiments with 50 mg of the composites in 50 ml solutions of phenol (concentrations up to 500 mg l^{-1} at pH 5), chloroform (concentrations up to 500 mg l^{-1}), chlorobenzene (concentrations up to 25 mg l^{-1}), and drimaren red dye (concentrations up to 100 mg l^{-1}). All the solutions were kept for 24 h at 25±1 °C in a temperature-controlled bath. The concentrations of volatile organic compounds (phenol, chloroform and chlorobenzene) were measured by MIMS (membrane introduction mass spectrometry) [19–22]. The concentration of red drimaren dye was measured by UV/vis spectrophotometry.

3. Results and discussion

3.1. Characterization of the composites

The composites were prepared by the precipitation of iron oxides or hydroxides onto a carbon surface. After preparation, a test with a 0.3 T magnet showed that the whole material was magnetic and completely attracted to the magnet. The magnetization measurements, Fe content, BET surface area and microporous volumes (t-plot method) obtained for the prepared composites are shown in Table 1.

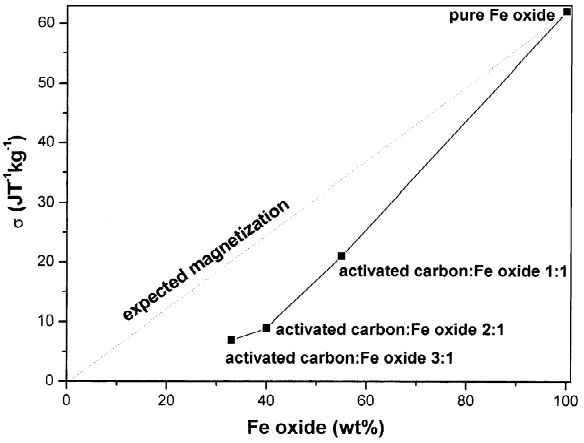

Fig. 1. Bulk sigma magnetization for different activated carbon/Fe oxide composites.

It can be observed from Table 1 that the bulk sigma magnetization increases for a higher Fe oxide content in the composite. However, this increase is not proportional to the Fe oxide content (Fig. 1), indicating that the concentration of non-magnetic iron oxides increases for the composites with higher activated carbon content. Four iron oxides are commonly formed under the reaction conditions employed, i.e. Fe_3O_4 (magnetite), γ-Fe_2O_3 (maghemite), α-Fe_2O_3 (hematite) and α-FeO(OH) (goethite) [23]. Among these oxides, only the first two, magnetite and maghemite, are magnetic with magnetizations of 100 and 60 J T^{-1} kg^{-1}, respectively [24]. Pure Fe oxide prepared without activated carbon showed a magnetization of 62 J T^{-1} kg^{-1}, which is similar to γ-Fe_2O_3, maghemite. Chemical analyses of pure Fe oxide showed an Fe^{3+}/Fe^{2+} ratio of approximately 7, which is much higher than the original ratio used ($Fe^{3+}/Fe^{2+} = 2$), probably due to

Table 1
Magnetization, BET surface area and microporosity measurements for the activated carbon/iron oxide composites

Composite	Bulk sigma magnetization (J T^{-1} kg^{-1})	Fe_2O_3 (wt%)	BET surface area (m^2 g^{-1})	$V_{microporous}$ (cm^3 g^{-1})
Pure Fe oxide	62	~100	66	0.010
Composite 1:1	21	47	–	–
Composite 2:1	9	33	626	0.172
Composite 3:1	7	25	658	0.177
Pure activated carbon	0	0	933	0.264

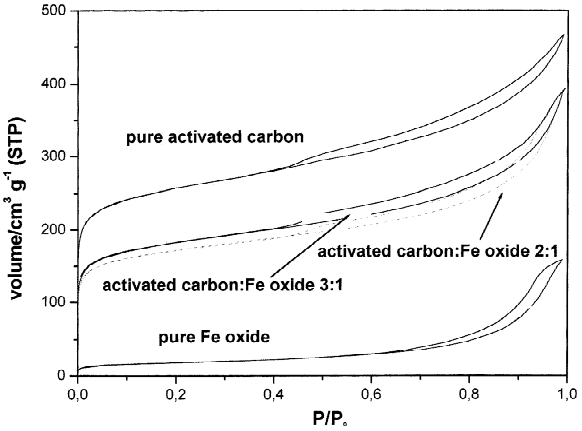

Fig. 2. Nitrogen adsorption–desorption isotherms for pure iron oxide, activated carbon and the composites.

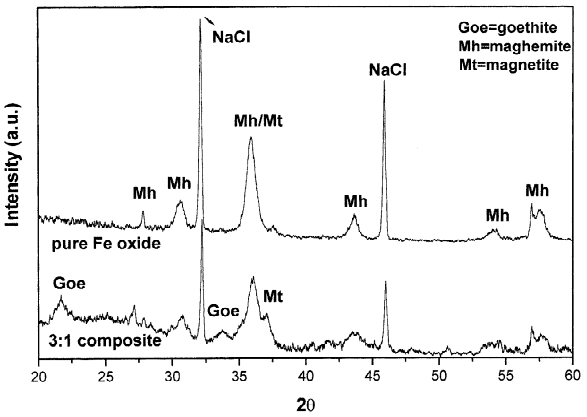

Fig. 3. Powder XRD for the 3:1 activated carbon/Fe oxide composite and pure Fe oxide.

oxidation of Fe^{2+} during preparation. These results suggest the formation of mainly Fe^{3+} compounds in the composite.

Fig. 2 shows the N_2 adsorption isotherms for pure iron oxide, pure activated carbon and for the prepared composites. The data shown in Table 1 suggest that the BET surface area and the microporous volume are not significantly affected by the presence of iron oxide in the composites. For example, for the 2:1 composite, reductions of the surface area from 933 (for pure activated carbon) to 626 $m^2\ g^{-1}$ and for the microporous volume from 0.264 to 0.172 $cm^3\ g^{-1}$ are observed. In both cases, the reductions of approximately 33% correspond to the decrease expected due to the presence of iron oxide in the 2:1 composite (33% iron oxide and 67% activated carbon). As iron oxide has a relatively small surface area and microporous volume (66 $m^2\ g^{-1}$ and 0.010 $cm^3\ g^{-1}$, respectively) its presence in the composites should cause a decrease in the surface area and microporous volume compared to pure activated carbon.

XRD analyses of pure Fe oxide (Fig. 3a) suggest the presence of a cubic iron oxide phase ($d = 2.50$, 2.91, 2.07, 1,60, 3.20 Å), which may be related to the presence of maghemite and also some magnetite. For the composite these peaks appear broader, suggesting a smaller crystallite size (ca. 25 nm for pure Fe oxide and 16 nm for the composite, obtained using Scherrer's equation [25]). Weak diffraction peaks are also observed at $d = 2.45$ and 2.70 Å, which may be related to the presence of small amounts of goethite and also some hematite.

The ^{57}Fe Mössbauer spectrum for the pure Fe oxide (Fig. 4a) at liquid N_2 temperature shows sextets with hyperfine fields of 47 and 48 T, suggesting the presence of an oxidized magnetite or maghemite structure. On the other hand, the Mössbauer spectra of the composite indicate the presence of a mixture of maghemite/magnetite and some goethite with hyperfine fields of 49, 46, 52 and 38 T [23].

Thermogravimetric analysis of the pure Fe oxide showed a weight loss due to water vapour of approximately 3% at temperatures lower the 100 °C. In the temperature range 120–180 °C a weight gain of ca. 0.3% is observed, which is likely related to the incorporation of oxygen due

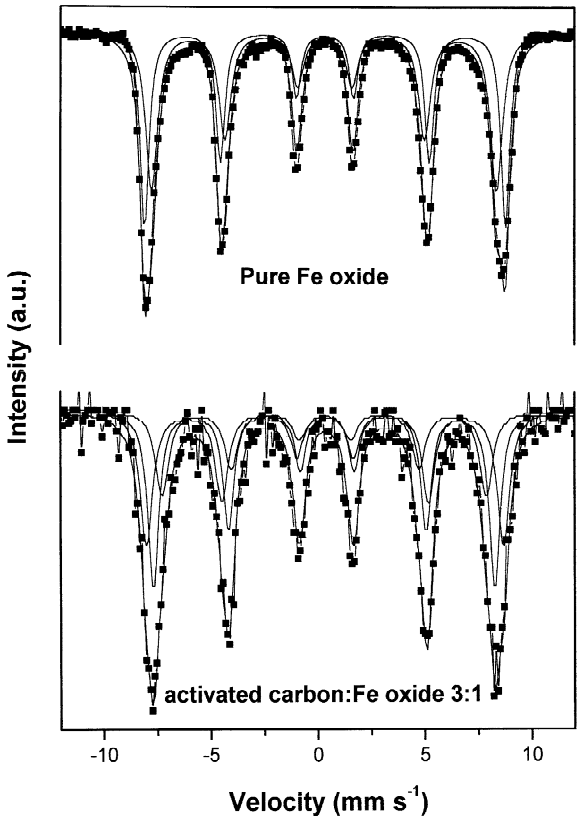

Fig. 4. Mössbauer spectra for the pure Fe oxide and the 3:1 activated carbon/Fe oxide composite at liquid N_2 temperature.

to the oxidation of Fe^{2+} to Fe^{3+} in the oxide [24]. The activated carbon/Fe oxide composite (Fig. 5b) showed weight loss due to water of ca. 10% up to 100 °C and a 65% weight loss from 350 to 500 °C related to the oxidation of the carbon. A weight of 25% is found after oxidation of the activated carbon, which is related to the Fe oxide in the 3:1 composite.

The temperature programmed reduction (TPR) profile of the prepared Fe oxide showed a peak centered at 450 °C with a shoulder at ca. 380 °C and a broad peak from 500 to 800 °C (Fig. 6a). XRD and Mössbauer analyses of the sample with the reduction interrupted after the first peak at 500 °C (Fig. 6b) showed the presence of mainly magnetite. This was corroborated by the increase in the bulk magnetization from 62 to 95 J T^{-1} kg^{-1}. After reduction at 900 °C, only pure Fe was detected by XRD, suggesting that the following reduction processes are taking place:

$$3Fe_2O_3 + H_2 = 2Fe_3O_4 + H_2O \quad T \cong 500\,°C \tag{1}$$

$$2Fe_3O_4 + 6H_2 = 6Fe^0 + 6H_2O \quad T > 800\,°C \tag{2}$$

Similar results were observed for the 2:1 activated carbon/Fe oxide composite (Fig. 6c), which showed a peak at 450 °C and a broad peak centered at ca. 750 °C.

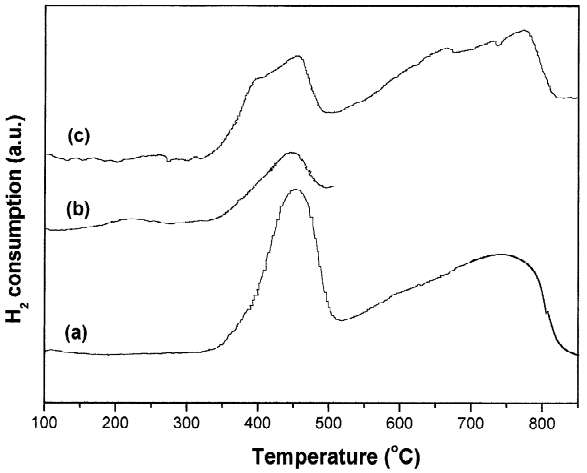

Fig. 6. TPR analyses for (a) the prepared Fe oxide, (b) the prepared Fe oxide interrupted at 500 °C and (c) the 3:1 activated carbon/Fe oxide composite.

XRD and Mössbauer analyses of the sample reduced up to 500 °C also showed the presence of mainly magnetite with the sample bulk magnetization increasing from 9 to 16 J T^{-1} kg^{-1}. These results suggest that, under controlled

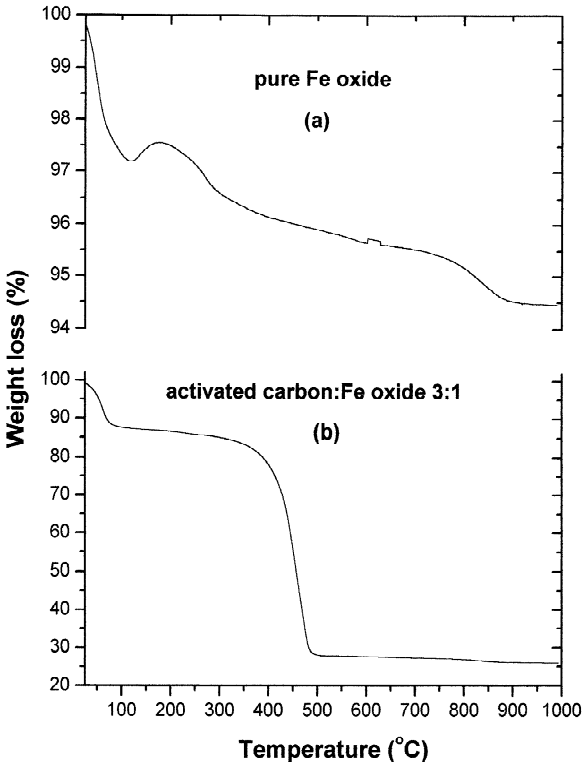

Fig. 5. Thermogravimetric analyses, in air, of pure Fe oxide (a) and the 3:1 activated carbon/Fe oxide composite (b).

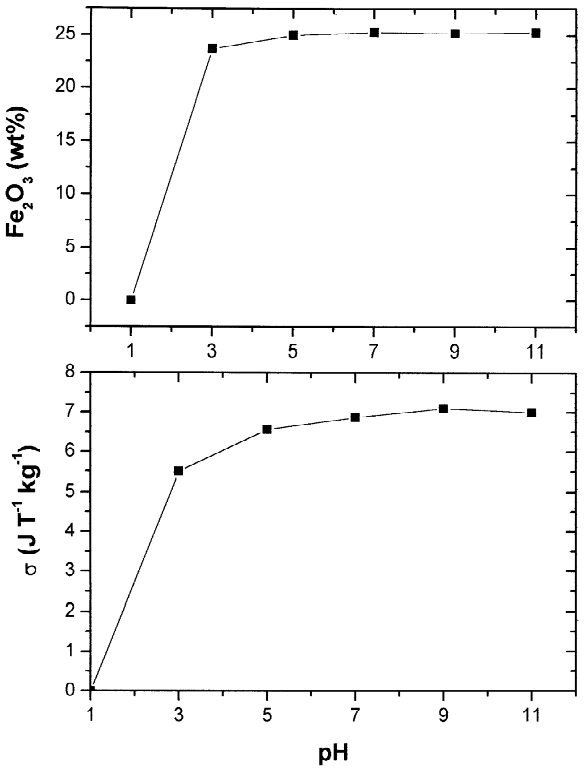

Fig. 7. Magnetization and Fe oxide content of the 3:1 activated carbon/Fe oxide composite exposed to pH 11, 9, 7, 5, 3 and 1 for 72 h.

conditions, non-magnetic iron oxides, such as hematite and goethite, and the magnetic maghemite can be reduced by hydrogen to produce magnetite. This controlled reduction enhances the magnetization of the composite, which is especially important to improve the magnetic separation of the absorbent after application.

The resistance of the composite to the acidity of the medium was also studied by exposing the 3:1 activated carbon/Fe oxide composite to pH 11, 9, 7, 5, 3 and 1 for 72 h. After this period the composite was dried and its magnetization and Fe oxide content were determined. The results are shown in Fig. 7.

There was no significant change in magnetization or Fe oxide content in the pH range 5–11. At pH 3, a small decrease in magnetization occurred, probably due to partial attack of the acid on the iron oxide, whereas treatment at pH 1 leads to complete dissolution of the Fe oxide with the destruction of the composite.

The morphologies of the 3:1 activated carbon/Fe oxide composite, activated carbon and the prepared Fe oxide were studied by SEM. The micrographs obtained for these materials are shown in Fig. 8a–c. Fig. 8a and b show general views of the composite. Small aggregates are observed, which appear brighter (indicated by arrows), supported on the darker surface of the activated carbon. Fig. 8c and d show details of the prepared Fe oxide aggregate and the pure activated carbon.

3.2. Adsorption of organic compounds

The adsorption of volatile organic compounds, i.e. phenol, chloroform and chlorobenzene, from aqueous

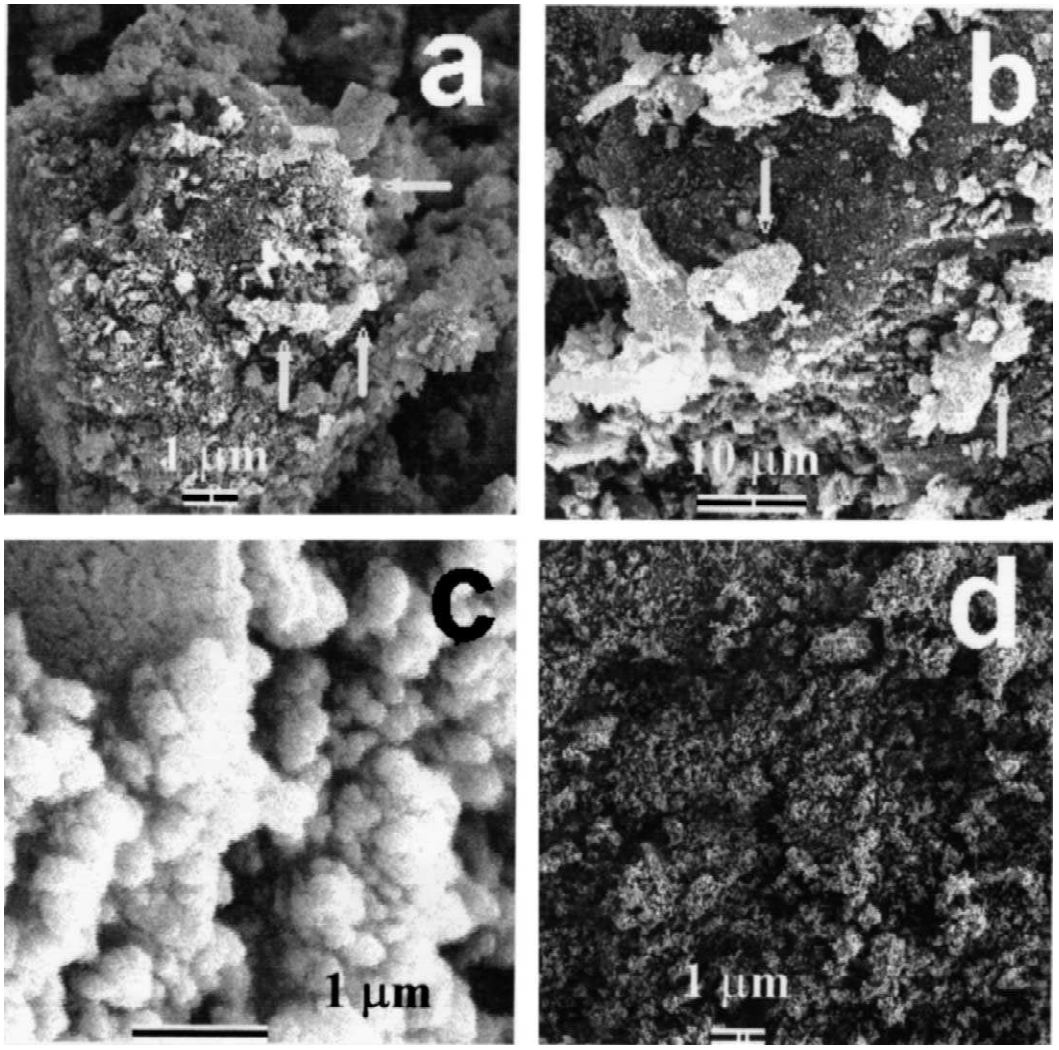

Fig. 8. SEM micrographs of (a) the 3:1 activated carbon/Fe oxide composite, (b) a detail of the composite, (c) pure Fe oxide and (d) pure activated carbon.

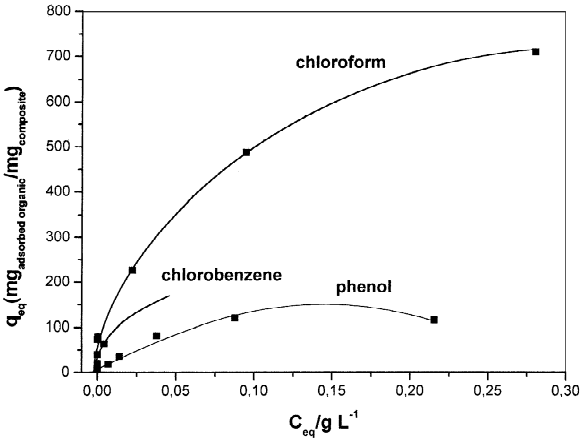

Fig. 9. Adsorption isotherms at 25±1 °C for phenol, chloroform and chlorobenzene over the 3:1 activated carbon/Fe oxide composite.

solutions onto the 3:1 activated carbon/Fe oxide composite was studied. The adsorption isotherms are shown in Fig. 9. It can be observed that the adsorption increases in the order phenol<chlorobenzene<chloroform with adsorption capacities of approximately, 117, 305 and 710 mg/$g_{composite}$, respectively. Experiments with pure activated carbon showed higher adsorption capacities of ca. 162, 480 and 910 mg/g_{comp} for phenol, chlorobenzene and chloroform, respectively. On the other hand, it is interesting to note that the presence of the iron oxide does not significantly affect the adsorption capacity of the activated carbon on the composite. The lower adsorption capacity of the composite is probably related to the small surface area of the iron oxide, which decreases the total surface area of the material to ca. 30% (Table 1) compared to pure activated carbon.

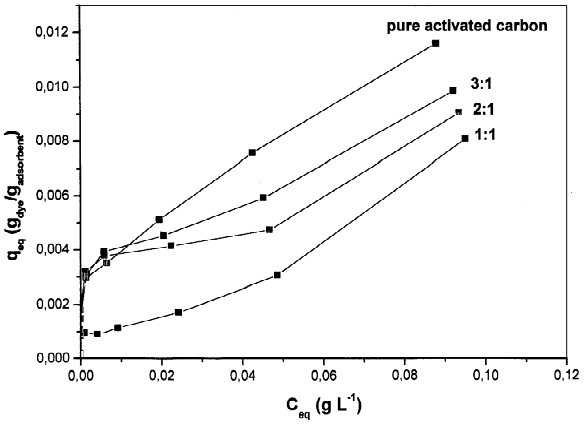

Fig. 10. Adsorption isotherms at 25±1 °C for drimaren red dye on the 3:1 and 2:1 activated carbon/Fe oxide composites and pure activated carbon.

The adsorption of drimaren red, a textile reactive dye, was also studied on pure activated carbon and on the 3:1 and 2:1 activated carbon/Fe oxide composites. The results (Fig. 10) show similar adsorption isotherms up to the equilibrium concentration of 0.01 g l^{-1}. At higher concentrations the isotherms obtained for the composites present a deviation from the typical Langmuir-type isotherm, which might be related to specific interactions of the reactive dye with the oxides. The adsorption capacity for the drimaren red dye decreases in the order activated carbon>3:1 composite>2:1 composite. This result is also probably related to the decrease in surface area caused by the presence of the iron oxide in the composite.

4. Conclusion

The magnetic composites reported in this work can be prepared with a high adsorption capacity activated carbon by a very simple procedure using available and low cost chemicals. Magnetization measurements, Fe^{3+}/Fe^{2+} ratios, XRD and Mössbauer data suggest that the main magnetic phase formed in the composites is maghemite, possibly with small amounts of magnetite, goethite and hematite. Controlled TPR experiments showed that the Fe_2O_3 oxides in the materials can be selectively reduced to produce magnetite, Fe_3O_4, enhancing the magnetization of the composites.

No significant decrease in the surface area or in the porosity of the activated carbon was caused by the presence of the Fe oxides in the composite. The composites showed high adsorption capacities for phenol, chloroform, chlorobenzene and drimaren red dye in aqueous solution and, more importantly, no reduction in adsorption was produced by the formation of the composite. Moreover, the magnetic composites showed good resistance over the pH range 5–11.

Acknowledgements

The authors are grateful to the CAPES/SCyT exchange program and to Prof. Wagner N. Mussel for valuable suggestions about the Mössbauer spectra.

References

[1] Booker NA, Keir D, Priestley A, Rithchie CD et al. Sewage clarification with magnetite particles. Water Sci Technol 1991;23(7–9):1703–12.
[2] Sing KS. Technology profile. Ground Water Monitor 1994;:60–76.
[3] Safarik I, Safarikova M, Buricova V. Sorption of water soluble organic dyes on magnetic poly(oxy-2,6-dimethyl-1,4-phenylene. Collect Czech Chem Commun 1995;60:1448–56.

[4] Orbell JD, Godhino L, Bigger SW, Nguyen TM et al. Oil spill remediation using magnetic particles. J Chem Educ 1997;74:1446.
[5] Pignon H, Brasquet C, La Cloirec P. Coupling ultrafiltration and adsorption onto activated carbon cloth: application to the treatment of highly coloured wastewaters. Water Sci Technol 2000;42(5/6):355–62.
[6] Lua AC, Guo J. Adsorption of sulfur dioxide on activated carbon from oil-palm waste. J Environ Eng ASCE 2001;127(10):889–94.
[7] Culp GL, Culp RL. New concepts in water purification, New York: Reinhold, 1974.
[8] Matson P, Mark HB. Activated carbon: surface chemistry and adsorption from solution, New York: Dekker, 1971.
[9] Ruthven DM. Principles of adsorption and adsorption processes, New York: Wiley, 1984.
[10] Baup S, Jaffre C, Wolbert D. Adsorption of pesticides onto granular activated carbon: determination of surface diffusivities using simple batch experiments. Adsorption 2000;6(3):219–28.
[11] Garner IA, Watson-Craik IA, Kirkwood R. Dual solute adsorption of 2,4,6-trichlorophenol and *N*-[2-(2,4,6-trichlorophenoxy)propyl]amine onto activated carbon. J Chem Technol Biotechnol 2001;76(9):932–40.
[12] Martín-Gullón I, Font R. Dynamic pesticide removal with activated carbon fibers. Water Res 2001;35(2):516–20.
[13] Jung M-W, Ahn K-H, Lee Y, Kim K-P, Rhee J-S. Adsorption characteristics of phenol and chlorophenols on granular activated carbons (GAC). Microchem J 2001;70(2):123–31.
[14] Denizli A, Özkan G, Uçar M. Removal of chlorophenols from aquatic systems with dye-affinity microbeads. Sep Purif Technol 2001;24(1/2):255–62.
[15] Aksu Z, Yener J. A comparative adsorption/biosorption study of mono-chlorinated phenols onto various sorbents. Waste Manage 2001;21(8):695–702.
[16] Daifullah AAM, Girgis BS. Removal of some substituted phenols by activated carbon obtained from agricultural waste. Water Res 1998;32(4):1169–77.
[17] Shim JW, Park SJ, Ryu SK. Effect of modification with HNO_3 and NaOH on metals adsorption by pitch-based activated carbon fiber. Carbon 2001;39(11):1635–42.
[18] Coey JMD, Cugat O, MaCauley J, Fabris JD. A portable soil magnetometer. Revista de Física Aplicada e Instrumental 1992;7:25–30.
[19] Augusti R, Diass AO, Rocha LL, Lago RM. Kinetics and mechanism of benzene derivatives degradation with Fenton's reagent in aqueous medium studied by MIMS. J Phys Chem A 1998;102:10723–7.
[20] Silva ACB, Augusti R, Dalmazio I, Windmoller D et al. MIMS pervaporation processes. Phys Chem Chem Phys 1999;1:2501–4.
[21] Kotiaho T, Kostiainen R, Ketola RA, Ojala M et al. Membrane inlet mass spectrometry: past and future. Adv Mass Spectrom 1999;14:501–27.
[22] Lauritsen FR, Kotiaho T. Advances in membrane inlet mass spectrometry. Rev Anal Chem 1996;15:237–65.
[23] Perez OP, Umetsu Y, Sasaki H. Precipitation and densification of magnetic iron compounds from aqueous solution at room temperature. Hydrometallurgy 1998;50:223–9.
[24] Oliveira LCA, Fabris JD, Mussel WN, Rios RVRA et al. The effect of Mn substitution on the catalytic properties of ferrites. Stud Surf Sci Catal 2000;130:2165–8.
[25] Cullity BD, editor, Elements of X-ray diffraction, Menlo Park: Addison-Wesley, 1978, pp. 123–31.

Journal of Catalysis **204,** 169–174 (2001)
doi:10.1006/jcat.2001.3373, available online at http://www.idealibrary.com on IDEAL®

The Structure of Carbon Encapsulated NiFe Nanoparticles

Wendy Teunissen,* Frank M. F. de Groot,*,[1] John Geus,* Odile Stephan,† Marcel Tence,† and Christian Colliex†,‡

*Debye Institute, Department of Inorganic Chemistry and Catalysis, Utrecht University, Sorbonnelaan 16, 3584 CA, Utrecht, The Netherlands; †Laboratoire de Physique des Solides, Bâtiment 510, CNRS UMR 8502, F 91405 Orsay, France; and ‡Laboratoire Aimé Cotton, Bâtiment 505, CNRS UPR 3321, F 91405 Orsay, France

Received April 26, 2001; revised June 26, 2001; accepted August 4, 2001

Carbon encapsulated NiFe nanoparticles (NiFe@C) have been prepared by high-temperature methane encapsulation of the bare bimetallic particles on alumina. High-resolution transmission electron microscopy pictures show that about 6-nm thick carbon layers encapsulate 10–20-nm diameter NiFe nanoparticles. The NiFe nanoparticles are shown to be single-crystalline and no carbide is found at the NiFe–C interface. This is confirmed by the electron energy-loss spectroscopy (EELS) measurements that in addition show that both Ni and Fe have a zero (metal) valence and that only graphite is present. EELS also shows that the nickel-to-iron ratio is exactly unity for all particles studied. Metallic Pd nanoparticles with a diameter of 1–2 nm can be anchored on the carbon layers, which creates a Pd/NiFe@C type of catalyst that could be used for liquid phase reactions. The EELS analysis reveals that part of the nanoparticles present are not Pd but other oxidic carbon encapsulated nanoparticles. © 2001 Academic Press

Key Words: **carbon encapsulation; TEM; EELS; magnetic separation.**

INTRODUCTION

A major goal in catalysis research is the development of small solid bodies that can be suspended in and extracted from the liquid phase. These bodies need to be small to overcome the transport limitations in the liquid phase. Bodies smaller than a few μm cannot be separated by filtration or centrifugation. Magnetic separation offers a route to use particles of about 50 nm, but requires these nanoparticles to have a sufficiently high saturation magnetization, while redispersion asks for magnetic softness. NiFe and CoFe bimetallic systems are satisfactory candidates from the magnetic point of view. For the particles to be used as catalytic support material, they must be inert and resistant to the conditions during catalytic reactions. Bare metallic nanoparticles certainly do not fulfill these requirements and a solution is the embedding of the bimetallic nanoparticles in carbon sheets.

Carbon encapsulation has attracted much attention after the discoveries of fullerenes, single-walled carbon tubes, and related systems (1, 2). Multiwalled carbon fibers, also known as carbon filaments, have a long history, ever since the 1889 patent on the growth of carbon filaments by metal crucibles (3). Throughout the twentieth century the nucleation and growth of carbon fibers has been an important field of research, mainly because of the destructive nature of carbon fibers on reactor walls (4, 5). The knowledge of the prevention of carbon fiber growth automatically yielded new insights on the optimization of carbon fiber growth modes and, closely related, on the growth of encapsulated metal particles (5).

EXPERIMENTAL

Carbon encapsulated NiFe particles (NiFe@C) have been prepared by (a) growing NiFe metal particles on γ-alumina, (b) encapsulating these NiFe metal particles in a methane flow, followed by removal of alumina and also any incompletely covered particles with an acid treatment, and (c) having Pd nanoparticles anchored on the outside of the carbon encapsulated particles. Compared to the arc discharge method (1, 6–9), as well as other methods (10–12), this catalytic route to the production of carbon encapsulated nanoparticles offers a much more detailed control of, for example, the alloy composition. In addition, scaleup is expected to be easier.

(a) The NiFe particles are prepared by depositing *sodium nitroferricyanide* ($Na_2Fe(CN)_5NO$) and *nickel nitrate* $Ni(NO_3)_2$ precursors, which have a nickel-to-iron ratio of 1 : 1. The aqueous iron cyanide solution is injected at a rate of 1 ml/min into a vigorously stirred suspension of γ-alumina in an aqueous solution of nickel nitrate and kept at pH 5. The NiFe loaded alumina was filtered, washed, and dried at room temperature in a vacuum for 24 h. The 425–850-μm sieve fraction was calcined in a 95 ml/min flow of 20% oxygen in helium at 573 K for 3 h. This gives NiFe–oxide particles on alumina. This treatment is followed by a reduction in a 100 ml/min flow of 20% hydrogen in argon

[1] To whom correspondence should be addressed. Fax: ++31 30 2511027. E-mail: f.m.f.degroot@chem.uu.nl.

0021-9517/01 $35.00
Copyright © 2001 by Academic Press
All rights of reproduction in any form reserved.

at 700°C for 2 h. This gives about 20 wt% bare NiFe alloy particles on γ-alumina (13, 14).

(b) The encapsulation procedure is based on the large body of knowledge developed for the growth of carbon fibers (5). The alloy particles were brought to 998 K under flowing hydrogen, exposed to a 100 ml/min flow of 20% methane in argon at 998 K for 1 h and cooled to room temperature in a flow of argon. This yields carbon encapsulated NiFe particles as well as partly uncovered alloy particles. To isolate the encapsulated NiFe particles, 200 mg of alumina was dissolved by boiling the sample with 50-ml concentrated hydrochloric acid for 30 min. 200 ml of cold demineralized water was added and the material was filtered, washed, and dried in air at room temperature. The acid treatment has removed all NiFe particles with porous carbon layers, in this way excluding the presence of nickel–iron alloy particles in not fully closed shells. The relative yield of the NiFe particles prepared in this manner is 68% (14).

(c) To prepare NiFe@C supported palladium catalysts, we used incipient wetness impregnation with $PdCl_2$ dissolved in hydrochloric acid. It turned out from previous research on carbon fibers that no further activation procedure is required for anchoring the palladium complex on the carbon (15, 16). The pore volume (voids between the spherical NiFe@C particles) of the material was measured to be 0.9 ml/g. To prepare a catalyst with a Pd loading of 2.5 wt%, NiFe@C was placed in an impregnation flask and brought under static vacuum. The calculated amount of the Pd solution was injected into the flask and kept under static vacuum for 15 min. Next, an argon flow was passed over at a temperature of 333 K for 1 h. The Pd complex anchored to the carbon layers was converted to metallic palladium upon reduction in hydrogen. Samples of Pd/NiFe@C were placed in a reactor in a gas flow of 10% H_2 in Ar, raising the temperature with 1.5 K/min to 473 K.

RESULTS AND DISCUSSION

The geometric and electronic structure of NiFe@C particles has been characterized with transmission electron microscopy (TEM) and electron energy-loss spectroscopy (EELS) using a scanning TEM. The TEM images were acquired with a Topcon 002B electron microscope operating at 200 kV, equipped with a LaB_6 filament, and providing a point resolution of about 0.2 nm. Samples were prepared by suspending the solid in ethanol under ultrasonic vibration. One or two drops of the thus prepared suspension were brought onto a punched carbon film on a copper grid. The EELS data were recorded with a scanning transmission electron microscope VG HB 501, equipped with a field-emission source and a parallel Gatan 666 EELS spectrometer. This instrument produces EELS spectra with a typical 0.7-eV resolution recorded from subnanometer areas

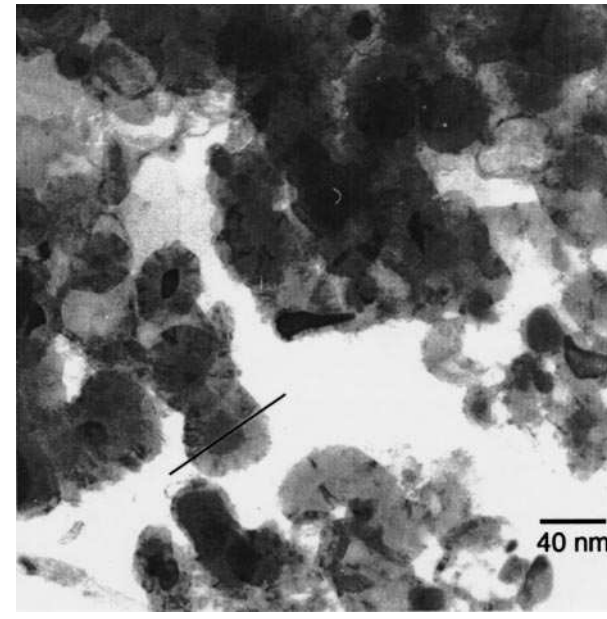

FIG. 1. TEM image of carbon coated nickel–iron particles. The line indicates the probe position during the EELS analyses.

(17, 18). In the line-spectrum mode, spectra are recorded while ramping the probe with given steps across the specimen. Acquisition times required for achieving a satisfactory signal-to-noise level on core edges are on the order of 100 ms–1 s. A checking of the materials after EELS measurements indicated that there was no radiation-induced structural damage.

A TEM picture of the particles is shown in Fig. 1. The metallic core is encapsulated in polyhedral concentric graphitic shells with a varying number of layers. Figure 2 shows a high-resolution photo of the lattices of the metallic core and the surrounding carbon. From this figure the lattice distance found for the NiFe core is 0.21 nm, in agreement with the (111) lattice dimension of metallic NiFe. For graphite we measured a lattice distance of 0.34 nm, close to its (002) lattice. All particles studied showed only one orientation of the NiFe lattice, without grain boundaries. This indicates that the particles measured are single crystals. As far as detectable from the images, no dissimilarity in the lattice distances are observed at the interface of the NiFe metal core and the carbon layers. This indicates that no carbidic phase is present, an observation that will be confirmed by the EELS measurements.

An EELS spectrum, taken at a probe position on the NiFe metal core is represented in Fig. 3. The electron, energy-loss fine structure of the carbon K edge at 280 eV, the iron $L_{2,3}$ edge at 710 eV, and nickel $L_{2,3}$ edge at 850 eV are clearly visible. The iron and nickel edges are much weaker than the carbon K edge and they have been multiplied by 8.0 in Fig. 3. The spectral shapes of the EELS core edges provide chemical information on the nature of the elements

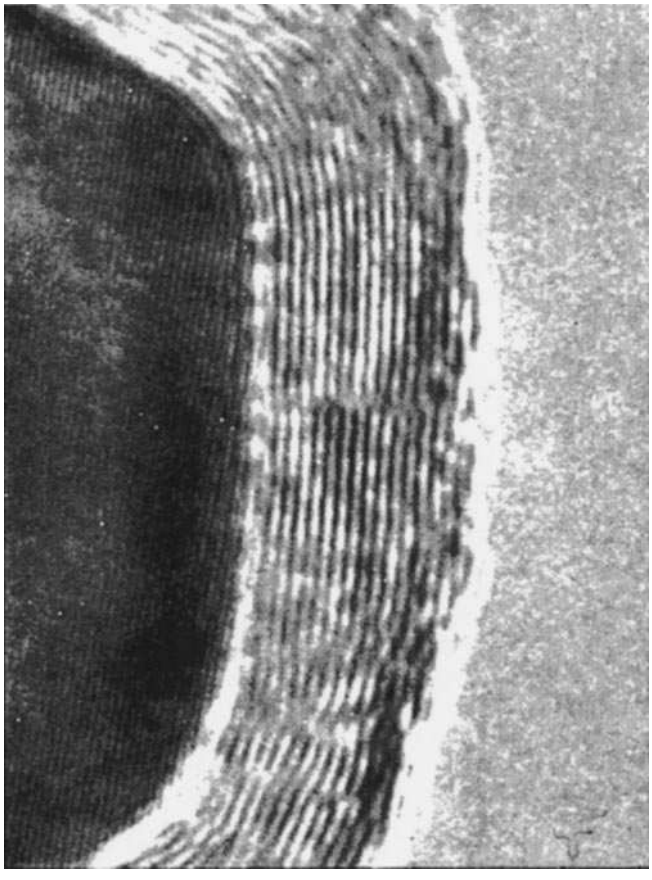

FIG. 2. High-resolution TEM image of the NiFe core and the surrounding graphite layers. The graphite layer thickness is approximately 6 nm.

(19, 20). The nickel and iron $L_{2,3}$ spectra (shown with better statistics in Fig. 5) indicate metallic nickel respectively iron (21), while the carbon K edge is reminiscent of graphitic carbon.

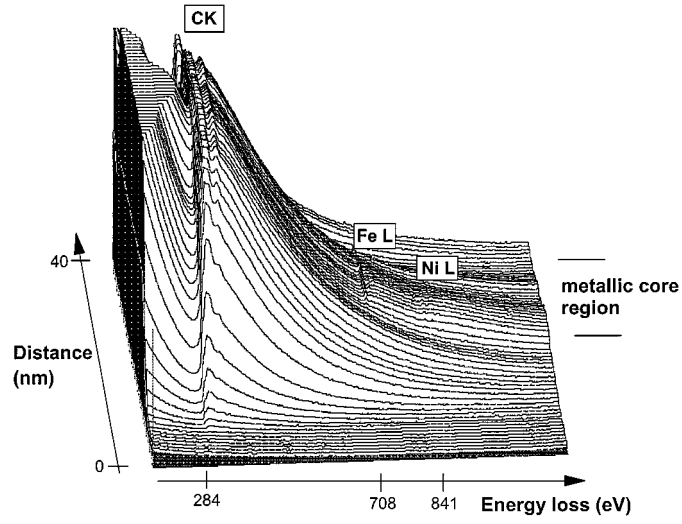

FIG. 4. 2D plot of a line spectrum (64 spectra) as the probe beam scans along a line of approximately 40 nm from vacuum through a 35-nm NiFe@C particle. Horizontal scans represent the energy-loss values.

Figure 4 represents the 2D plot of a sequence of spectra taken across a particle of about 35 nm with a metallic core of about 12 nm. The path was chosen through the center of the particle as indicated in Fig. 1. The sequence of 64 spectra was recorded with a 0.5-nm probe, a 0.6-nm pixel increment, and an acquisition time of 1 s per pixel. This amounts to a total path length of 40 nm within a total acquisition time of 64 s. To obtain the nickel-to-iron ratio within the alloy particle, the cross sections of the carbon K edge, nickel L edge, and iron L edge were estimated for every EELS spectrum. Figure 5 shows part of one EELS spectrum. The region used for background subtraction is indicated before the iron and nickel edges and the resulting background is given as the

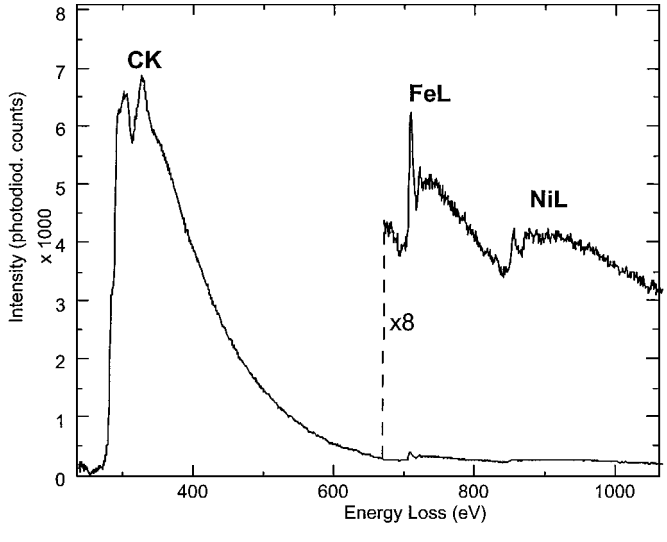

FIG. 3. Electron energy loss fine structure of the carbon K edge and the iron and nickel L edge. The spectrum is taken at one probe position.

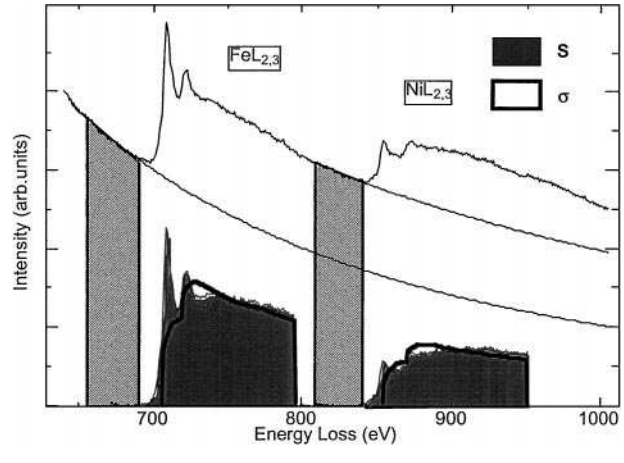

FIG. 5. $L_{2,3}$ edges for iron and nickel recorded from carbon encapsulated particles. Also shown are the two characteristic signals after background subtraction, the energy window for integration of the characteristic signals and calculated ionization cross sections, and the calculated atomic cross sections calculated in a Hartree–Slater model.

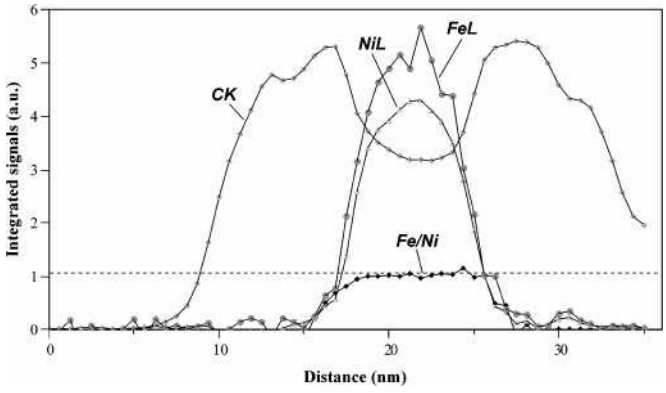

FIG. 6. The normalized intensity variations of the carbon K, nickel $L_{2,3}$, and iron $L_{2,3}$ edges as the beam is scanned across an encapsulated NiFe particle.

thin lines. The characteristic signals after background subtraction are shown with filled surfaces, indicating also the energy window for integration of the characteristic signals and the calculated ionization cross sections (22). In order to improve the statistics and limit potential sample damage, we did measure the EELS spectra over the core level region only; i.e., the plasmon region was not detected in parallel. We note that this has the disadvantage that for thick samples it is not possible to correct the intensity profile for multiple scattering events.

The results of the analysis have been summarized in Fig. 6. No elements other than carbon, nickel, and iron were detected. As the beam scans across the particle, the intensity of the energy-loss peaks corresponding with the K edge in graphite (window: 280–325 eV) increases corresponding with the increasing number of carbon atoms in the column that the beam encounters, exhibits a drop in the center due to the internal hollow space, and follows the same pattern on the other side. The shape of the profile essentially shows a cylindrical geometry (23), which is in agreement with a small slice in the center of a spherical particle projected in a two-dimensional way. A distortion from a perfect hollow sphere can be observed in the small dip around the position at 14 nm. This indicates that the graphitic layer deviates from a perfect sphere. The intensity of the energy loss from the $L_{2,3}$ edges of nickel and iron correlates well with the position of the central core of the particle and the peaking of intensity in the center clearly indicates that the alloyed nickel and iron is present as a solid sphere and is not just wetting the inside surface. An elemental quantification using tabulated atomic 2p ionization cross sections (24) gives a constant ratio of nickel and iron very close to unity, in agreement with the adjusted nickel-to-iron ratio in the cyanide complex used during preparation, namely $NiFe(CN)_5NO$. A similar result was found for all six investigated particles. In summary, the shape of the different curves in Fig. 6 confirms the approximately spherical geometry of the particle, with a hollow core for carbon, filled with a solid core with a nickel-to-iron ratio of unity.

No spectral variations were found across the iron and nickel $L_{2,3}$ edges in the particle core and also at the interface with graphite. The iron and nickel spectral shapes (cf. Fig. 5) indicate that both are present in their metallic state (21). The carbon K edge indicated in Fig. 3 corresponds to graphite and shows no indication for the presence of any carbidic species in the filled portion of the particle. The high-temperature synthesis of the surrounding graphite layers seems to result in nonsegregated, NiFe alloy particles encapsulated by closed shells of pure graphite with the absence of carbides at the interface. However, the comment must be made that a carbidic phase formed during synthesis, not finally resulting in nonporous surrounding graphitic layers, will be removed during treatment in hydrochloric acid. This result confirms the HRTEM images (cf. Fig. 2), where also no indication was found for a carbidic phase.

Anchoring of Pd Particles

A TEM micrograph of a NiFe@C-supported palladium catalyst after reduction is represented in Fig. 7. Clearly visible are the small particles on the external edge of the carbon layers. Most of these particles turned out to be metallic Pd, but as will be discussed below other types of small particles were found from the EELS analysis. The large particles are the ferromagnetic NiFe cores of the support. Apart from small particles on the outside of the NiFe@C particles, also small particles are visible at other positions in the sample,

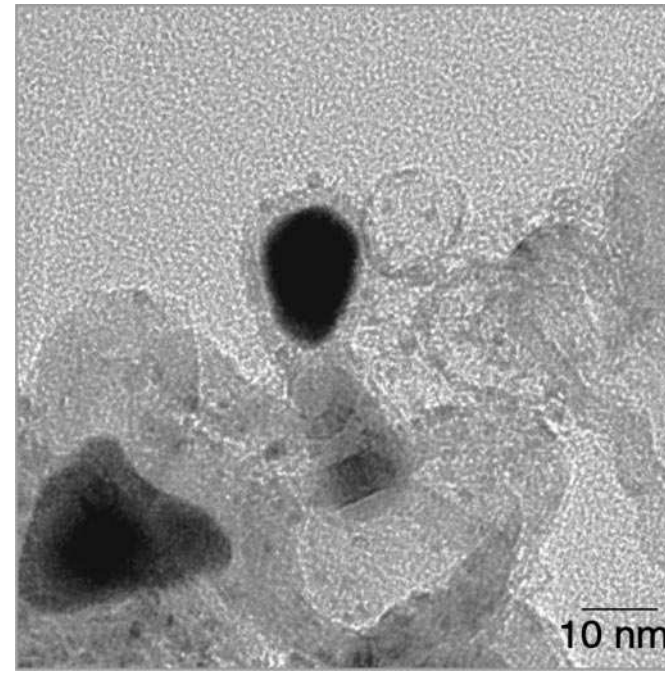

FIG. 7. TEM images of palladium on NiFe@C, prepared via impregnation.

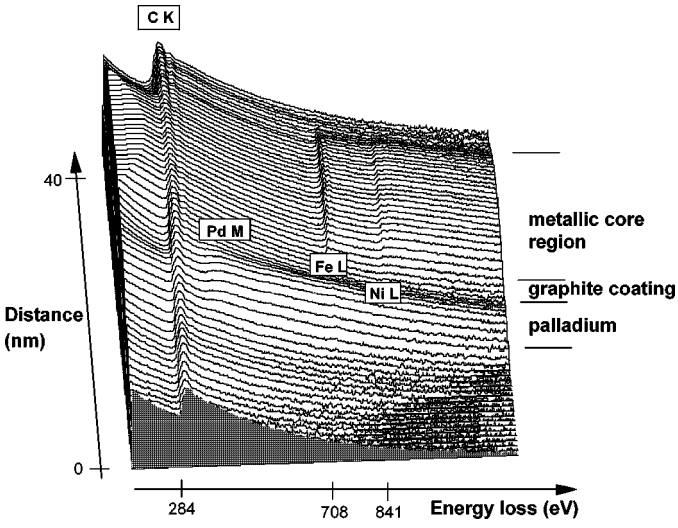

FIG. 8. 2D plot of a line spectrum along a line of approximately 40 nm from vacuum through a 60-nm Pd/NiFe@C particle. Horizontal scans represent the energy-loss values.

for example, on the empty sphere to the right of the NiFe@C particle.

Figure 8 shows the 2D plot of a sequence of spectra taken halfway across a particle of about 60 nm with a metallic core of about 40 nm. The sequence was recorded in the same manner as Fig. 4. In addition to the carbon K edge at 280 eV, the iron $L_{2,3}$ edge at 710 eV, and the nickel $L_{2,3}$ edge at 850 eV, the Pd $M_{2,3}$ edge at 532 eV can be observed. Figure 9 displays the profile of the relative intensities of Pd, C, Ni, and Fe calculated from the line scan shown in Fig. 8 and using the same procedure as described above for the NiFe@C particles. The carbon profile of Fig. 9 agrees with an almost perfect hollow spherical carbon particle. Palladium is located on the external edge of the particle, anchored to the carbon layers. A particle with a diameter of approximately 5 nm is found in Fig. 9. The spectral shape of the Pd $M_{2,3}$ edge shows that Pd is in its metallic state. However, we should mention that the detection of a small amount of oxygen is complicated due to the presence of the Pd M_3 edge in the O K energy range. We were not able to detect any deviation of the Pd or C spectra at the Pd/C interface, but we cannot rule out detection limitations due to the very small interface area. The iron-to-nickel ratio is constant throughout the particle, but deviates from the adjusted 1 : 1 ratio.

All particles with a NiFe core less than 12 nm in diameter show exactly the 1 : 1 ratio. Therefore we believe that this deviation is due to the incorrect background modeling and the consequent incorrect evaluation of the characteristic absorption signals. As indicated above, we did not measure the plasmon region of the EELS spectrum simultaneously, which excludes the elimination of multiple scattering effects. The Ni : Fe ratio in Fig. 9 is still found to be constant over the core of particle. This ratio seems to increase in the carbon region between the NiFe core and palladium nanoparticle. However, as the absolute Ni and Fe intensities decrease in this region, the uncertainty in the ratio increases and the determined value is not reliable enough to draw a firm conclusion.

A systematic scan on all small particles that are observable with EELS in a certain area showed that only about half of these particles consisted of Pd. Some of the small particles we examined turned out to be iron oxide or nickel–iron oxide, fully covered with graphite, where in some cases also aluminium is present. In Fig. 10 the EELS spectrum is shown of the analysis of a nickel–iron oxide particle, obtained by using the gain variation routine in the derivative mode. The particles found can originate from the interlayer between the metal and alumina support, which often is hard to reduce. With the formation of encapsulating graphite

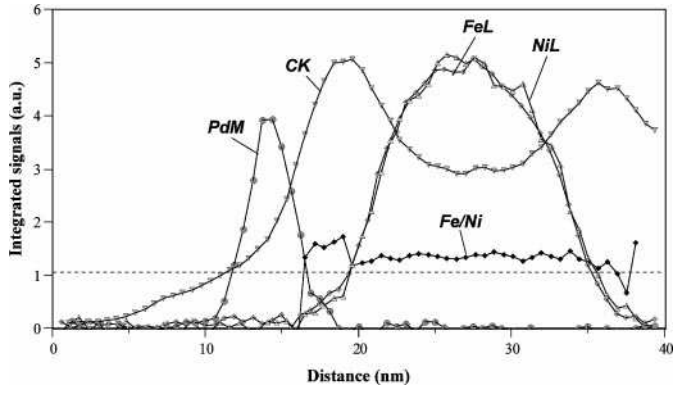

FIG. 9. The variation of intensity of carbon K, palladium $M_{2,3}$, nickel $L_{2,3}$, and iron $L_{2,3}$ edges as the beam is scanned across a Pd/NiFe@C particle.

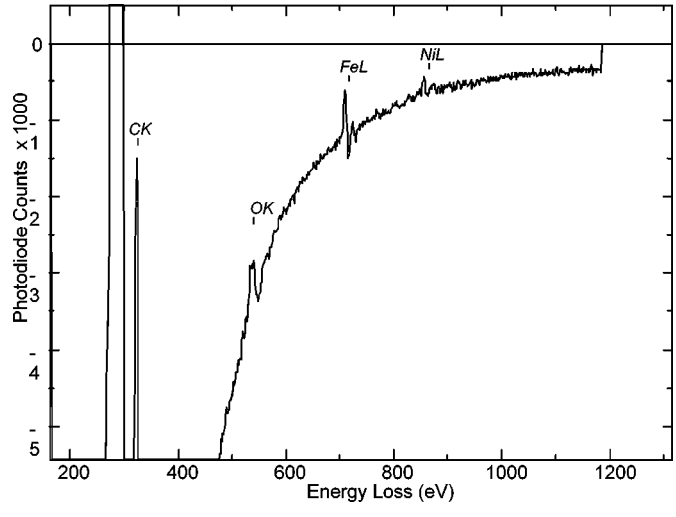

FIG. 10. Electron energy-loss fine structure of the carbon K edge, the oxygen K edge, and the iron and nickel $L_{2,3}$ edge. The spectrum is obtained using the gain variation routine, recorded in the derivative mode.

layers the interaction between the alloy particles and support has to be overcome. We suggest that the interface be broken up, leaving some particles in the oxidic phase which become fully encapsulated. These iron oxide, or nickel–iron oxide, encapsulated particles will also be present in the sample where no palladium is anchored to the NiFe@C particles. However, in a TEM picture a palladium nanoparticle of 2 nm will be better visible than a 2-nm NiFe–oxide particle. It is only with an EELS analysis that these nanoparticles reveal their elemental nature.

CONCLUSIONS

It can be concluded that TEM–EELS provides a detailed picture of the nature of the carbon encapsulated metal particles. The EELS intensity profiles reveal the relative ratio of the elements present. It should be noted that EELS intensity profiles have a spatial resolution of approximately 0.5 nm, which is intrinsically much better than the resolution that can be obtained from an EDX elemental analysis. The EELS elemental analysis is quantitatively correct for thin samples. For samples with a thickness larger than about 30 nm, EELS can also yield quantitatively correct values if the values are corrected for multiple scattering events. The high spatial resolution of the EELS spectra has been used to study potential chemical interface effects. These effects were not observed with the resolution of 0.5 nm.

The NiFe core is found to be metallic and single-crystalline with a lattice distance equal to bulk NiFe and with exactly a 1 : 1 Ni : Fe ratio. The diameter of the particles varies between 10 and 30 nm. The particle is encapsulated by graphitic planes with an interplanar distance equal to bulk graphite. The graphite forms a hollow sphere around the NiFe nanoparticle and no carbidic interface between the metal core and the graphite is visible.

We conclude that the preparation method for anchoring small Pd particles to carbon encapsulated NiFe particles is very effective. This keeps alive promises for the development of encapsulated metal particles as catalyst support materials that can be suspended in, magnetically extracted from, and redispersed in the liquid phase.

Half of the small nanoparticles observed in TEM are related to carbon encapsulated oxides, which is a result that could only be obtained from the EELS analysis. It would be very hard to distinguish such oxidic particles from the Pd particles using TEM only.

ACKNOWLEDGMENTS

This work was carried out as part of the Innovation Oriented Research Programme on Catalysis (IOP Catalysis IKA94080) sponsored by the Netherlands Ministry of Economic Affairs. The research of FdG has been supported by the Netherlands Research Combination Catalysis.

REFERENCES

1. Kratschmer, W., Lamb, L. D., Fostiropoulos, K., and Huffman, D. R., *Nature* **347**, 354 (1990).
2. Iijima, S., *Nature* **354**, 56 (1991).
3. Hughes, T. V., and Chambers, C. R., U.S. Patent 405, 480 (1889).
4. Rostrup-Nielsen, J. R., *J. Catal.* **85**, 31 (1984).
5. de Jong, K. P., and Geus, J. W., *Chem. Eng. Rev. Sci. Eng.* **42**, 481 (2000).
6. Dravid, V. P., Host, J. J., Teng, M. H., Elliot, B., Hwang, J., Johnson, D. L., Mason, T. O., and Weertman, J. R., *Nature* **374**, 602 (1995).
7. Scott, J. H. J., and Majetlich, S. A., *Phys. Rev. B* **52**, 12,564 (1995).
8. Dong, X. L., Zhang, Z. D., Jin, S. R., and Kim, B. K., *J. Appl. Phys.* **86**, 6701 (1999).
9. Sun, X., Gutierrez, A., Yacaman, M. J., Dong, X. L., and Jin, S., *Mat. Sci. Eng. A* **286**, 157 (2000).
10. Nolan, P. E., Lynch, D. C., and Cutler, A. H., *J. Phys. Chem. B* **102**, 4165 (1998).
11. Nolan, P. E., Lynch, D. C., and Cutler, A. H., *Carbon* **31**, 817 (1996).
12. Harris, P. J. F., and Tsang, S. C., *Chem. Phys. Lett.* **293**, 53 (1998).
13. Teunissen, W., and Geus, J. W., *Stud. Surf. Sci. Catal.* **121**, 185 (1998).
14. Teunissen, W., Bol, A. A., and Geus, J. W., *Catal. Today* **48**, 329 (1999); Wendy Teunissen, Ph.D. thesis. Utrecht University, Utrecht, The Netherlands, 2000.
15. Hoogenraad, M. S., van Leeuwarden, R. A. G. M. M., van Breda Vriesman, G. J. B., Broersma, A., van Dillen, A. J., and Geus, J. W., *Stud. Surf. Sci. Catal.* **91**, 263 (1995).
16. Mojet, B. L., Hoogenraad, M. S., van Dillen, A. J., Geus, J. W., and Koningsberger, D. C., *J. Chem. Soc. Faraday Trans.* **93**, 4371 (1997).
17. Jeanguillaume, C., and Colliex, C., *Ultramicroscopy* **28**, 252 (1989).
18. Colliex, C., Tencé, M., Lefèvre, E., Mory, C., Gu, H., Bouchet, D., and Jeanguillaume, C., *Mikrochim. Acta* **71**, 114 (1994).
19. Colliex, C., *in* "NATO ASI Series, Series B: Physics" (P. S. Bagus, G. Pacchioni, and F. Parmigiani, Eds.), Vol. 345, p. 213, Colliex, C., *J. Electron. Microsc.* **45**, 44 (1996).
20. de Groot, F. M. F., *J. Elec. Spectrosc.* **67**, 529 (1994).
21. Fink, J., Müller-Heinzerling, Th., Scheerer, B., Speier, W., Hillebrecht, F. U., Fuggle, J. C., Zaanen, J., and Sawatzky, G. A., *Phys. Rev. B* **32**, 4899 (1985).
22. Egerton, R. F., *in* "Electron Energy-Loss Spectroscopy in the Electron Microscope." Plenum, New York, 1986.
23. Suenaga, K., Colliex, C., Demoncy, N., Loiseau, A., Pascard, H., and Williame, F., *Science* **278**, 653 (1997).
24. Leapman, R. D., Rez, P., and Mayers, D. F., *J. Chem. Phys.* **72**, 1232 (1980).